Universidad de Concepción
Dirección de Postgrado
Facultad de Ciencias Físicas y Matemáticas
Programa de Magíster en Ciencias Mención en Fisíca

PRIMER ANÁLISIS QUÍMICO DEL CÚMULO ABIERTO DE EDAD INTERMEDIA IC 166 (FIRST CHEMICAL ANALYSIS OF THE INTERMEDIATE-AGE OPEN CLUSTER IC 166)

Tesis para optar al grado de Magíster en ciencias con mención en Física

JOSÉ LUIS SCHIAPPACASSE ULLOA
CONCEPCIÓN - CHILE
2017

Profesor Guía: Dr. Douglas Geisler
Departamento de Astronomía, FCFM
Universidad de Concepción

UNIVERSIDAD DE CONCEPCIÓN

Resumen

Facultad de Ciencias Físicas y Matemáticas
Departamento de Astronomía

Primer análisis químico del cúmulo abierto de edad intermedia IC 166

por José Schiappacasse Ulloa

Los cúmulos abiertos son unos de los mejores trazadores de la química y la dinámica del disco galáctico debido a su homogeneidad comparado a las estrellas del campo. La mayoría de los cúmulos abiertos no puede sobrevivir en el energético disco galáctico por mucho tiempo, por lo que cúmulos abiertos de edad intermedia y viejos son extremadamente valiosos para investigaciones científicas. El cúmulo abierto de edad intermedia, IC 166, está profundamente enterrado en el disco galáctico, y ha sido pobremente estudiado. Desde APOGEE DR14, confirmamos 13 probables miembros de IC 166 usando sus ubicaciones, metalicidades, velocidades radiales y movimientos propios. También confirmamos, desde el diagrama color-magnitud, que ellos son probablemente estrellas red clump. Nosotros estudiamos las abundancias químicas y cinemática de los miembros del cúmulo para obtener una completa visión química-dinámica del cúmulo. Manualmete analizamos las abundancias químicas (incluyendo Mg, Si, Ca, Ti, Al, K, Mn y Fe) de los miembros del cúmulo usando el código BACCHUS y comparamos con los resultados de ASPCAP. Nuestros resultados derivados manualmente son similares a los resultados de ASPCAP para la mayoría de los elementos con posibles pequeños desfaces, excepto para Al. La gran dispersión de [Al/Fe] presentada por los resultados de ASPCAP es significantemente reducida por nuestro análisis manual. También realizamos simulaciones de su órbita usando el código de dinámica galáctica GravPot16. Nuestros resultados químicos y cinemáticos sugieren que IC 166 es un cúmulo abierto típico del disco delgado.

UNIVERSIDAD DE CONCEPCIÓN

Abstract

Facultad de Ciencias Físicas y Matemáticas
Departamento de Astronomía

First chemical analysis of the intermediate-age open cluster IC 166

by José Schiappacasse Ulloa

Open clusters are one of the best chemical and dynamical tracers of the Galactic disk, due to their homogeneity compared to field stars. Most of the open clusters cannot survive in the energetic Galactic disk for long, therefore intermediate-age and old open clusters are extremely valuable to trace the earliest epochs of the disk formation and evolution. The intermediate-age open cluster IC 166 is buried deeply in the Galactic disk, and was poorly studied until now, in large part due to its significant obscuration in the optical. From APOGEE DR14, we confirm 13 likely cluster member for IC 166 using their cluster location, metallicity, radial velocity, and proper motion. We also confirm that they are likely red clump stars from the color-magnitude diagram. We study the chemical abundances and dynamics of the cluster members to derive a comprehensive chemodynamical view of this cluster. We manually analyze the chemical abundances (including Mg, Si, Ca, Ti, Al, K, Mn and Fe) of the IC 166 cluster members using the BACCHUS code and compare with the ASPCAP results. Our manually derived results are similar to the ASPCAP results for most elements with possible small offsets, except Al. The large [Al/Fe] spread presented in the ASPCAP results is significantly reduced in our manual analysis. We also perform orbit simulations using our Galactic dynamic code GravPot16. Our chemical and dynamical results suggest IC 166 is a typical thin disk open cluster.

Contents

List of Figures

List of Tables

Chapter 1

Introduction

1.1 A brief overview

In the Milky Way (MW) we can find different types of stars with different ages, different metallicities and different masses. We know that more massive stars will have shorter lifetimes than their less massive counterparts, so the lifetime of a given star is strongly determined by its mass. On the other hand, in general, we find that older stars are more metal poor - termed population II (pop-II)- and younger stars are more metal rich - known as population I (pop-I). There is yet another type of population for even more metal poor, older stars than pop-II stars, called population III (pop-III).

The most accepted model suggests that density waves produce gravitational instabilities in interstellar clouds triggering successive contractions and fragmentations of the molecular cloud which finally lead to the formation of hundreds or even thousands of stars. So, probably all stars that we can see in the dark sky were born in associations or clusters or at least most of them.

From the previous paragraph we define a star cluster is a gravitational bound system which is constituted by star with a common origin. We can conclude that each star of a cluster or association was formed from the same molecular cloud and for this reason they share a similar chemical composition (assuming the cloud is well mixed), thus we can assume that reflect the chemical composition of the progenitor molecular cloud . Additionally, they were formed almost at the same time so they share a similar age. These two features (same age and composition) define a simple stellar population (SSP), making star clusters unmatched tools for studying stellar evolution.

There are three types of cluster clearly differentiable for their pronounced characteristics such as their morphologies, sizes, gravitational binding energies and population types inside of them. They are very powerful tools to study a wide variety of astrophysical

phenomena in our Galaxy as well as other galaxies.
In the following section we will describe those interesting objects from their members, lifetimes and their importance in the galactic context.

1.1.1 Globular cluster (GC)

Their name is derived from the circular shape of this cluster type. They are characterized as pop II and are located mainly in the halo and bulge of the MW. They are massive objects with a typical mass of a few hundred thousand solar masses. GCs are the oldest objects in our galaxy with a range age between about 10 to ∼13 Gyr. (see Fig.1.1)
They have classically been used as prototype SSPs, but over the last decade or 2 gathering evidence shows that many/most/all of them do not satisfy the basic requirement of initial chemical homogeneity. Carretta et al. (2009) for first time shows -in a large sample- some anomalies in their chemical patterns such as Na-O anti-correlation that reflect at least two different stellar populations in GCs, so now GCs define what is termed multiple stellar populations (MPP) because these different populations do not share the same chemical composition and/or age. One of the theories that explain these anomalies tell us that the first generation of stars pollutes the pristine material of the cluster from winds of asymptotic giant branch (AGB) stars and SN explosions which are retained by the cluster and which enrich the interstellar medium with heavy elements processed inside the stars. A second generation(s) of enriched stars is then formed in the cluster center at a later time.

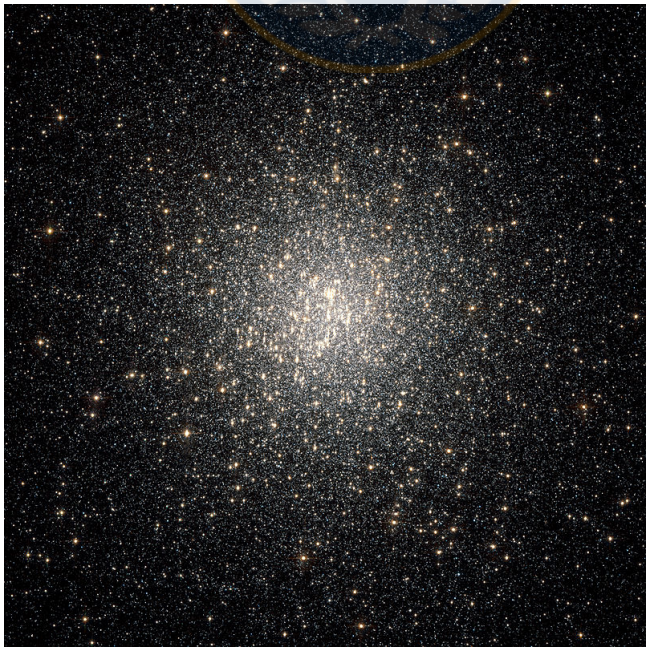

FIGURE 1.1: NGC 2808: One of the most massive GCs. Source: ESO/T. Preibisch

1.1.2 OB associations

While they are not a true cluster, being gravitationally unbound, the do provide important information about the spiral arms where they were born. The notorious presence of O and B stars (several to tens of stars per cluster) is the main characteristic of this stellar group. They are not a gravitationally bound system. Due to the short lifetime of the O and B stars they cannot live live more than a few Myr so they can not get too far from their birthplace. For this reason OB associations are very useful tracers of the sites of star formation and the morphology of the galaxies. The life of these massive stars ends with a supernova explosion which is responsible for the early chemical enrichment of the interstellar medium (ISM) over very large area around the exploded star (see Fig.1.2[1])

FIGURE 1.2: OB association in Carina nebula. Source: ESO/T. Preibisch

But, we need to describe one type of cluster more, the type of object where we will focus our efforts. They are open clusters (OCs) (see Fig.1.3) and will be described in the next section.

1.2 Open Clusters

OCs are scarcely gravitationally bound systems with a relative low star density. Inside of them we can find typically between hundreds to tens of thousands stars. They cover a wide age range between a few Myr and almost the age of the disk such as the extreme case of NGC 6791 with ∼8 Gyr, they also can be found in every part of the galactic disk, so in general, OCs are strongly obscured by the dust between our line of sight and them, making difficult their study, especially in the optical. In addition, general crowding in the disk makes differentiation between cluster and field stars in the same line of sight

[1]http://www.eso.org/public/images/eso1208a/ credits: ESO/T. Preibisch

problematic. It is estimated that there are more than 25,000 OCs in our Galaxy, but for the reasons previously mentioned, we have just studied around 1,000 of them.
The fact that the OCs are located throughout the entire galactic disk and that their age extends from very young clusters (even still forming) to those as old as the disk itself, makes it possible to study, for example, the metallicity and α-elements gradients along the disk. Also, OCs are powerful tools to study star formation, stellar evolution, nucleosynthesis, chemical enrichment and in this way, constrain models. Basically, we can say that OCs are excellent tracers of the history (formation and evolution) of the galactic disk.
In this section will be described OCs in different aspects, in order to make a global picture of those objects.

FIGURE 1.3: 30 new OCs of the MW discovered using VISTA infrared survey. Source: ESO/J. Borissova

1.2.1 Classification of Open Clusters

The classification of OCs (see Fig:1.4[2]) is based on their appearance and was defined by Trumpler (1930), thus it is also known as the *Trumpler classification*. The 3 different criteria used by Trumpler will be described below:

- Degree of central concentration: According to the degree of concentration of the stars in the cluster will be assigned a roman numeral.
  - **I:** OCs with heavily central concentration of stars.
  - **II:** OCs with moderately central concentration of stars.

[2]http://www.astrophoton.com/trumpler_class.htm

- **III:** OCs with weakly central concentration of stars.
- **IV:** OCs with a not clear concentration. It is difficult to distinguish with field stars.

- Range of brightness: According to the quantity of bright and faint stars in the cluster will be measured on a scale between 1 and 3.
  - **1:** Most of the stars in the cluster have a similar brightness. Mainly fainter stars.
  - **2:** The stars in the cluster have a moderate brightness.
  - **3:** There are a few bright stars mixed with moderate and faint stars.
- Quantity of stars: According to the number of the stars that belong to the cluster will be assigned three different letters.
  - **p:** This letter denotes a poorly populated OC (less than 50 stars).
  - **m:** This letter denotes a moderately populated OC (between 50 and 100 stars).
  - **r:** This letter denotes a rich populated OC (more than 100 stars).

Additionally, the letter **'n'** can be attached to this classification when the OC has a nebula associated with it. The latter is a clear difference with GCs which have a lack of stellar formation.

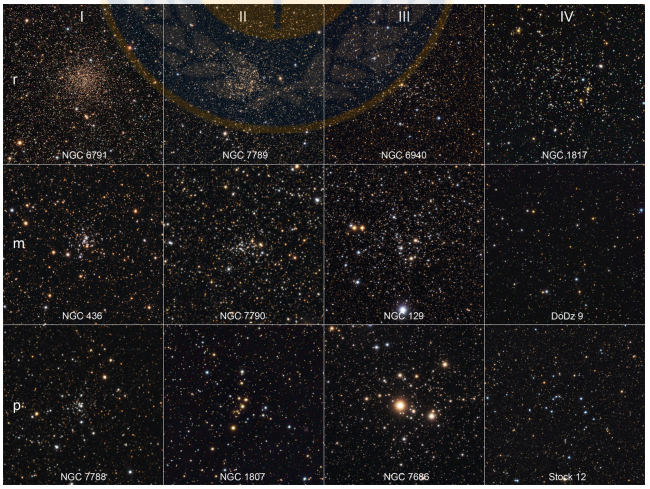

FIGURE 1.4: Scheme with different OCs and their respective classification. All these clusters have a brightness range 2 and 3. OCs names are labels. Source: WEBDA (Lynga catalogue)

1.2.2 Color Magnitude Diagram

One of the most powerful photometric tools for the study of OCs properties is the color magnitude diagram (CMD) that in the case of the OCs is mainly constituted, in the

youngest ones, by main sequence (MS), binaries and blue stragglers stars and, in the oldest ones, stars in evolved stages. Using OCs CMDs we can also learn about their reddening, distance and age fitting isochrones, so the CMDs studies can be a key piece of evidence for their understanding.

Due to the fact that binary stars form a parallel sequence to the MS reaching up 0.75 magnitudes brighter than the MS, and that blue straggler stars often occur in the bluer part of the turn-off point (TOP) –point where a star deviates from the MS and shows the end of the Hydrogen-burning core– which makes to OC look younger than it really is, we have to be careful in fitting isochrones in order to get reliable cluster properties.

The Fig.1.5 was taken from Sandage (1957) and shows a CMDs compilation for different OCs. It is clear that OCs with TOP in brighter magnitudes are related with minor age and, on the other hand, OCs with a TOP in fainter magnitudes are related to older clusters and, obviously, to evolved stars.

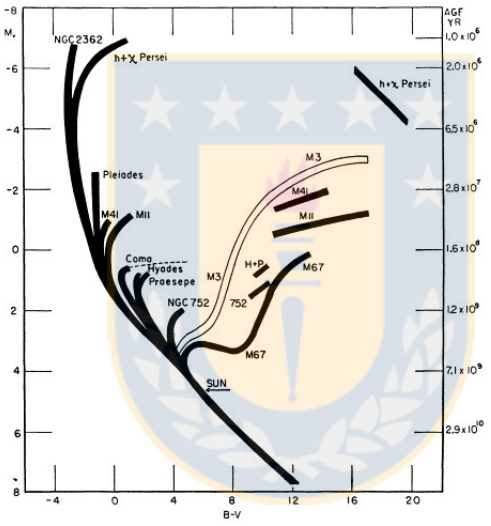

FIGURE 1.5: A compilation of OCs CMD is shown. Also a GC was included. Additionally, ages at the indicated on the right axis, derived from the absolute magnitude of the TOP. Source: Sandage (1957)

1.2.3 Size and Morphology

While GCs have a spherical distribution, the OCs morphology can be varied. There are OCs highly populated and centrally concentrated and, on the other hand, less populated OCs with an irregular shape.

Important morphological concepts are the following: the core radius is defined as the radius where the density of the cluster falls to the half of the cluster's central density. On the other hand, the tidal radius is defined as the radius where the cluster's members are more gravitationally influenced by external effects that by the cluster itself.

Commonly, for OCs, the core radii has values close to 1 or 2 parsec (pc), while the tidal

radii has values between 10 and 25 pc which, for GCs, can reach up to 10 times this value. Even tough there is not a strong correlation between the size and age of the OC, van den Bergh (2006) found that the oldest clusters generally are larger than the youngest ones. However, it is also possible to find large OCs amongst the youngest ones (a few Myr) due to the fact that after their formation, they begin to expand until they reach their equilibrium (Lada & Lada, 2003).

1.2.4 Mass and Age

As noted before, OCs extend over a wide range in both mass and age. While the smallest OCs can have a mass of only about 10 $M_{\odot}$, the most massive OCs have an upper mass limit of a few 10^4 $M_{\odot}$. On the other hand, while OC formation is ongoing inside of the spiral arms of the MW, most of the OCs have an age of several hundred Myr and just a few of them overcome the barrier of 1 Gyr.

In general, a more massive OCs can survive longer. Some N-body simulations have been realized in order to understand the dynamical evolution caused by both internal and external effects in the OCs. As was shown by Mathieu (1984), Moraux et al. (2004) and other efforts, during an OCs lifetime mass segregation occurs, which consists in the displacement of the more massive stars toward the center of the cluster and the migration of less massive stars toward the tidal radii and beyond, triggering a mass loss at an early age in the cluster. The mass segregation could lead to the dissolution of most of the cluster in a few Gyr, but as was shown by Spitzer (1958) the disruption can be accelerated also by external effects such as tidal forces and interaction with giant molecular clouds (GMC).

Hurley et al. (2005) tried to model the current features of M67 using a N-body simulation, finding that the cluster has lost almost 90% of its initial mass after 4 Gyr, as was expected, caused by mass segregation and the encounters with GMC.

For these reasons, the interest in the oldest OCs (older than Hyades) lie in their advanced ages. Additionally, it is important to know how they have evolve and their evolution and under what conditions they can reach those ages. Also, with their help we can have a better understanding about, for example, chemical abundances and chemical gradients in the early stages of the disk.

1.2.5 Distribution in the MW

For many decades, it has been known that OCs are located in the galactic disk close to their birthplace. For this reason, it is logical that these objects received the name 'Open Galactic Clusters'.

But the detailed distribution of OCs is not as simple as originally assumed. Using a large sample of OCs, (Janes et al., 1988) determined that the spatial distribution correlated with the cluster age. This means that, on average, there is an increase in the OCs age as we move away from the galactic center.

Bonatto et al. (2006), using a larger and improved sample, confirmed the results from previous efforts. A view from the top of the MW shows the OCs distribution in the disk (see Fig.1.6). While the youngest ones can be found throughout the entire disk, this is not the same for oldest ones that are practically absent inside of the solar circle. However, even these samples are fraught with selection effects, especially towards the galactic center due to dust extinction, so we need to wait for new samples in this zone of the galaxy in order to get more reliable conclusions.

In addition, a correlation between the age of OCs and the vertical height above the plane exists. Bonatto et al. (2006) showed that the youngest OCs are mainly concentrated to low altitude, while their older counterparts are located up to higher altitude which help them to have a greater longevity, since they avoid their disruption due to encounters with GMC.

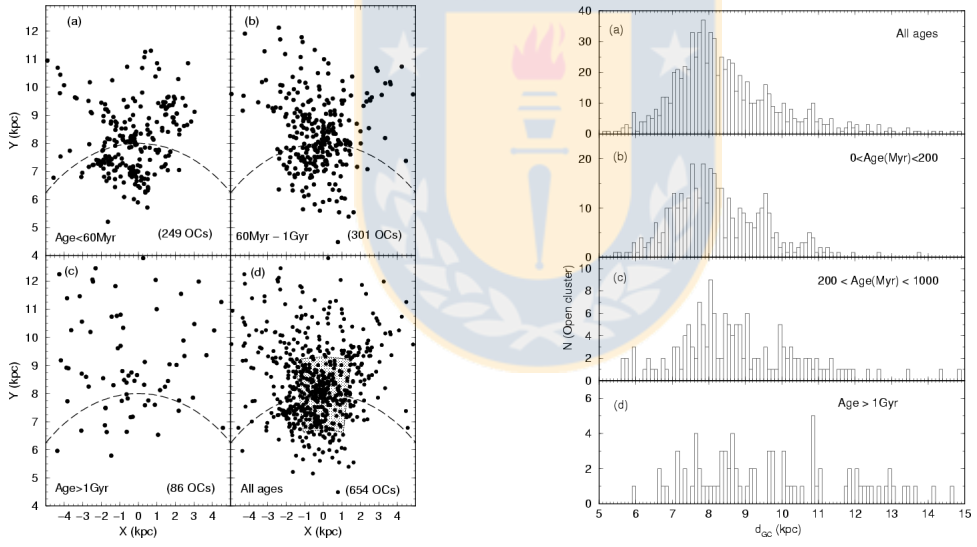

FIGURE 1.6: Left: A view from the top of the MW showing the OCs distribution separated for different age range. Dashed line represent the solar radii. Right: An histogram about the OCs distribution along the disk separated for ages. Source: Bonatto et al. (2006).

Summarizing, both Open and Globular clusters have remarkable and distinct features such us shape, distribution in the MW, but also -as was shown by Carretta et al. (2010)- they have different distributions of masses and ages (see Figure 1.7). In this Figure, the Globular clusters are mostly concentrated to higher masses and ages compared to Open cluster (open circles).

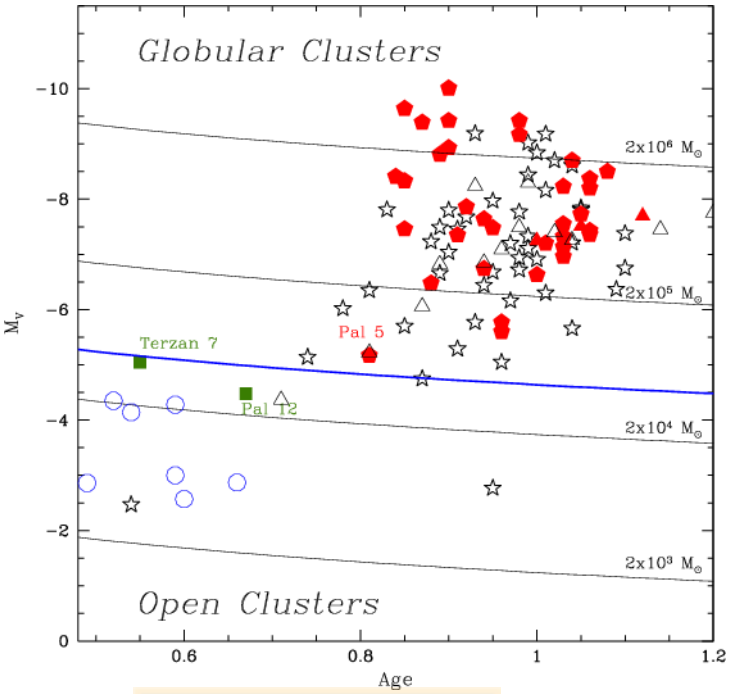

FIGURE 1.7: M_V-Age plane: As is shown in Carretta et al. (2010), it is possible to distinguish the different types of clusters present in the Milky Way. Source: Carretta et al. (2010)

1.3 APOGEE

In order to unravel the mysteries of Galaxy formation through a precise and systematic large-scale kinematic and chemical study, Apache Point Observatory Galactic Evolution Experiment (APOGEE) (Majewski et al., 2017) was accepted as part of Sloan Digital Sky Survey III (SDSS-III).

In its first version, using the Sloan Foundation 2.5m Telescope (Gunn et al., 2006) (see Fig.1.8) located at Apache Point Observatory in south east New Mexico, APOGEE started its observations in the spring of 2011, having a duration of three years. After this successful campaign, and SDSS team decided to expand it to the southern hemisphere using the Irénée du Pont 2.5-m Telescope (Bowen & Vaughan, 1973) (see Fig.1.9), located at Las Campanas Observatory in northern Chile, for this aim.

Currently, this project's extension is called APOGEE-2. Being part of the SDSS-IV, this project started its observations in the fall of 2014 and will finish in the fall of 2020. Using both telescopes, APOGEE will be able to observe the entire MW (see Fig.1.10).

But, what exactly is APOGEE? APOGEE is a near-infrared spectroscopic survey which will observe 300,000 stars with a high spectral resolution (R∼22,500) working in a wavelength range between 1.51 μm and 1.70 μm (H-Band) reaching a signal to noise ratio (S/N) >100 per pixel. All these features make it an excellent tool mainly for observations of the disk and bulge where the optical light of the stars is strongly affected by the extinction, so this survey allows us to study the populations hidden by the galactic dust.

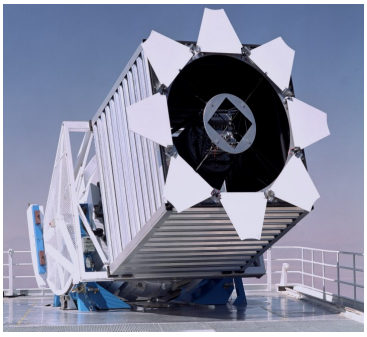

FIGURE 1.8: Sloan Foundation 2.5m Telescope. Source: Apache Point Observatory

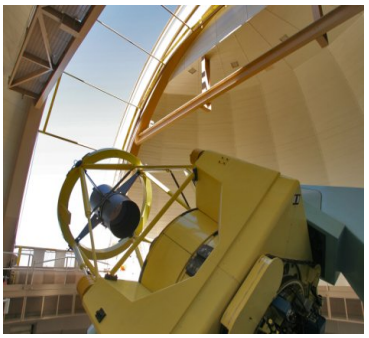

FIGURE 1.9: Irénée du Pont 2.5-m Telescope. Source: Las Campanas Observatory

In order to complete a global perspective of the MW, APOGEE also observes the halo.

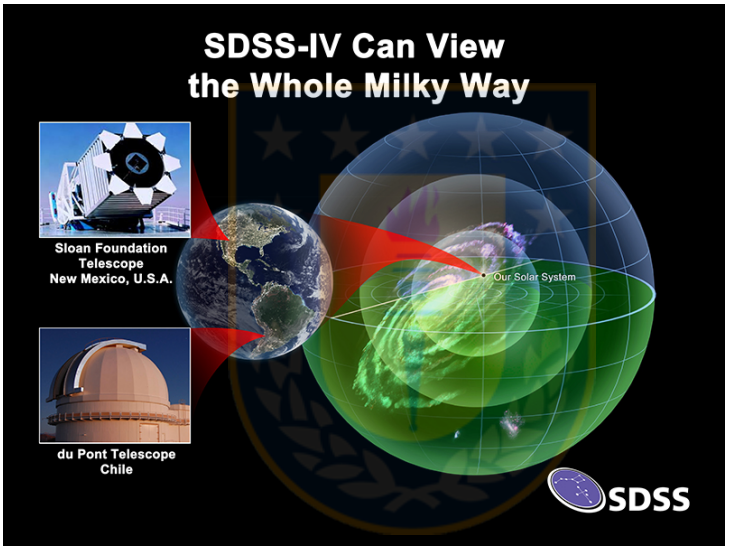

FIGURE 1.10: The observations of the Iréné du Pont and Sloan Foundation telescopes will allow APOGEE to get a homogeneous, global vision of the whole Galaxy. Source: Dana Berry / SkyWorks Digital Inc. and the SDSS collaboration

Surveys like APOGEE are a great advantage for astronomers due to the increasingly large and precise systematic and homogeneous samples. Specifically, APOGEE reaches an element abundance precision of ∼0.1 dex for 25 different species (C, C I, N, O, Na, Mg, Al, Si, P, S, K, Ca, Ti, Ti II, V, Cr, Mn, Fe, Co, Ni, Cu, Ge, Rb, Y, Nd), which allows both a complete chemical evolution study and chemical enrichment probe of the MW. Additionally, APOGEE gives us a radial velocity precision of ∼200 ms^{-1}, which allows detailed kinematic studies, useful to constrain evolutionary models of the MW, e.g.

1.3.1 Knowing APOGEE

The question is, how can a ground-based survey achieve such precision and quality in its data? APOGEE uses a method that involves various aspects including the spectrograph, target selection and visits, to the the data reduction pipeline, and finally to the chemical abundance pipeline (ASPCAP), which derives the stellar parameters and determines the abundances using model atmospheres, all adding to the overall strategy of observation. All of these, working together, make APOGEE a powerful observational tool. Some aspects are described further below:

- **Spectrograph:** APOGEE spectrograph is able to record 300 different spectra at the same time. The light is carried from the telescope to the spectrograph using 300 fibers. Each have a field of view of 2 arcsec on the sky (see Fig.1.11).

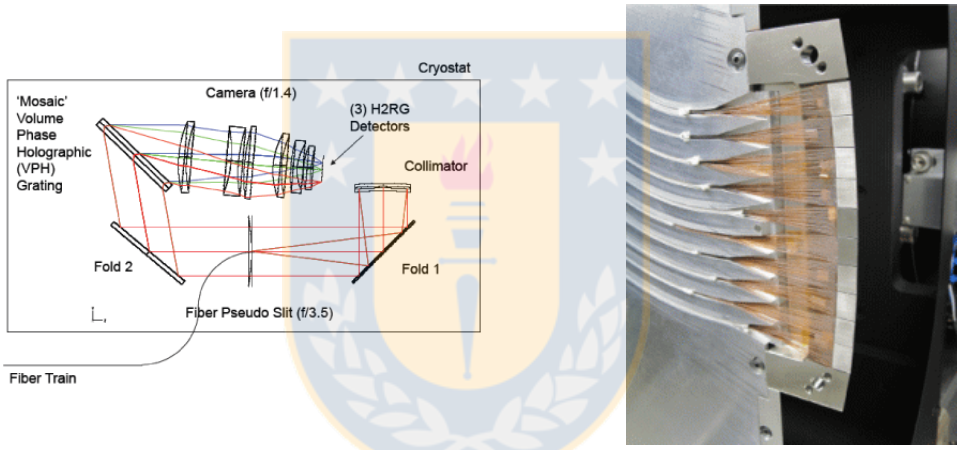

FIGURE 1.11: APOGEE spectrograph scheme (left). Source: SDSS III. Fibers carrying the light from the telescope to the spectrograph (right). Source: SDSS III

- **Target selection and fields:** APOGEE has a field of view of 7 deg^2. It targets a large number of fields in the Galactic thin disk, thick disk, bulge and halo (see Fig.1.12). Photometry from 2MASS is used by APOGEE in order to pick cool stars. A large percentage of the targets are in evolved stages such as the red giant branch (RGB), asymptotic giant branch (AGB) and red clump (RC). The observations are obtained in the H-band. This is a distinct advantage for the detection of faint stars because its 6 times less affected by the extinction than visual bands. For this reason APOGEE can reach stars with magnitudes between $7.0 > H > 13.8$ depending on the number of visits made to the field. Additionally, APOGEE observes 'special targets' with other goals e.g, stars with abundances and parameters known from previous works or numerous targets of ancillary scientific projects.

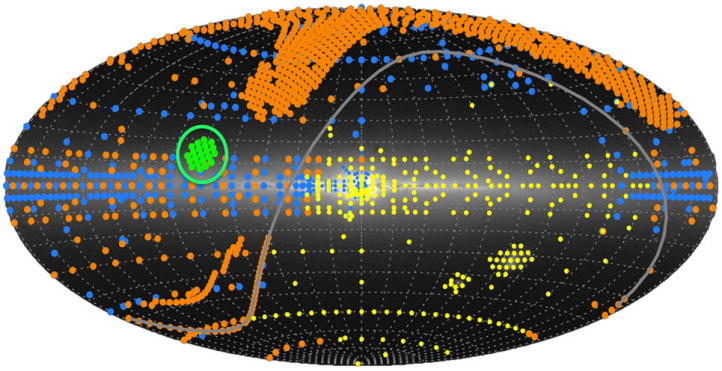

FIGURE 1.12: APOGEE fields in the galactic disk, bulge and halo. Blue, yellow and orange dots represent observation fields for APOGEE-1, APOGEE-2S and APOGEE-2N respectively. Finally, green dots are astroseismology and other fields. Source: APOGEE-2 | SDSS

- **Visits:** Each field should be observed at least once, but the majority of them are observed more than once in different nights. So, a visit is referred to as a single observation of a given field. Finally, different spectra from different visits of a particular star are combined in order to get a final spectra which is run through the ASPCAP. This method allows us 1) observe fainter stars (H$\sim$ 13.8 for 24 visits) and 2) identify binary stars systems as a result of radial velocity variations.

- **ASPCAP:** As is described by García Pérez et al. (2016) the pipeline automates the derivation of, first, the stellar parameters (effective temperature, surface gravity, microturbulent velocity and metallicity) by deriving the best fit to the whole spectrum. Is important to note that for a best fit, in this part, APOGEE takes into account C, N, O and α elements abundances due to the strong molecular absorption (CO, OH, CN) in the near-infrared (NIR).
  After getting the stellar parameters, APOGEE measures the chemical abundances from spectral windows for individual elements. In order to get these results, comparisons between libraries of theoretical and observed spectra are performed employing χ^2 minimization in a multidimensional parameter space reaching an accuracy $<$0.1 of dex.

In order to get the best chemical abundances possible, APOGEE perform some calibrations to the stellar parameters. Some of these are described below:

- **Effective Temperature ($\mathbf{T}_{eff}$):** It is calibrated comparing with photometric temperatures using stars with low extinction and includes a metallicity dependence.

- **Surface Gravity:** It is calibrated comparing with asteroseismic gravities which depend on the metallicity of the star. Is important to note that this calibration is different for RC and RGB stars.

- **Metallicity ([M/H]) and [α/M]:** Both are calibrated using observations of GCs and OCs. In general, the raw measurements from ASPCAP have small offsets that depend on the metallicity of the star.

Finally, the data reduced with stellar parameters, chemical abundances and radial velocities measured for every star are listed in two different catalogs in Flexible Image Transport System (FITS) format:

- **allVisit:** Catalog composed mainly by every visit performed to every star, including radial velocities of every visit. Specially useful for binary systems detection.
- **allStar:** Catalog composed mainly by information obtained from combined spectra of every star such as mean radial velocity, stellar parameters and chemical abundances.

The data are available for the users through two ways. 1) Using the databases tables in the SDSS catalog archive server (CAS) or 2) the data can be downloaded to the user's computer and managed easily using different programming languages e.g IDL or PYTHON. Some examples are available in the APOGEE webpage.
It is important to note that the reliability of the chemical abundances can change from one element to another because they depend on different aspects such as the features of each elemental absorption line, S/N or stellar parameters. Even some elements are in non-local thermodynamic equilibrium (NLTE) which can cause some errors in the measurements. These aspects will be discussed later.

1.3.2 Science with APOGEE

APOGEE with its large and homogeneous sample makes the work easier to modern astronomers, bringing benefits and new scientific knowledge. Here are presented some astronomical uses for APOGEE data.

- **Binary system detection:** The visits regime makes possible anomalies detected in the spectra of the stars produced in binaries systems (see Fig.1.13 /image from Majewski et al. (2017)).
- **Exoplanets detection:** APOGEE can reach radial velocity (RV) precision of $\sim$100 ms^{-1} which can be useful for exoplanets detection, as demonstrated by Fleming et al. (2015).

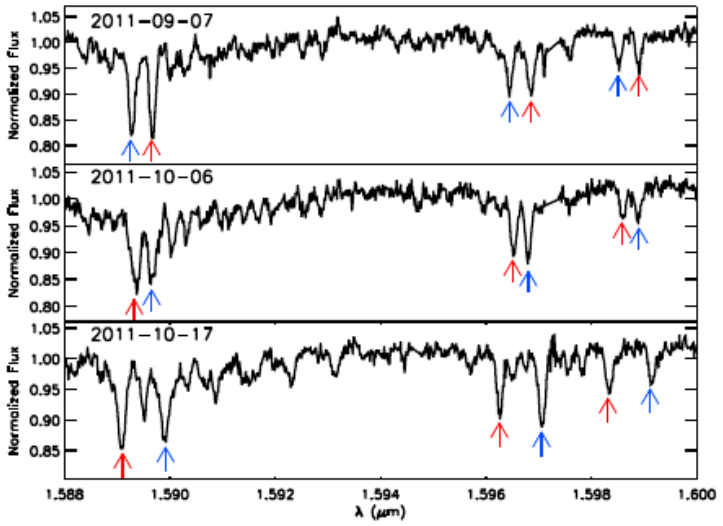

FIGURE 1.13: Spectra of a binary system take in different epochs. The absorption lines are duplicated and moving relative to each other with time due to orbital motion. Source: Majewski et al. (2017)

- **Multiple population in GCs:** The large chemical species measured by APOGEE makes possible the detection of multiple population in GCs through correlation or anti-correlations between some elements (see Fig.1.14 /image from Tang et al. (2017)).

- **OCs like tracers:** One of the most important targets of APOGEE are stellar population studies. In this sense, OCs can prove a powerful tool for the investigation of the dynamics and chemistry present in the galactic disk. This work will be an example of this.

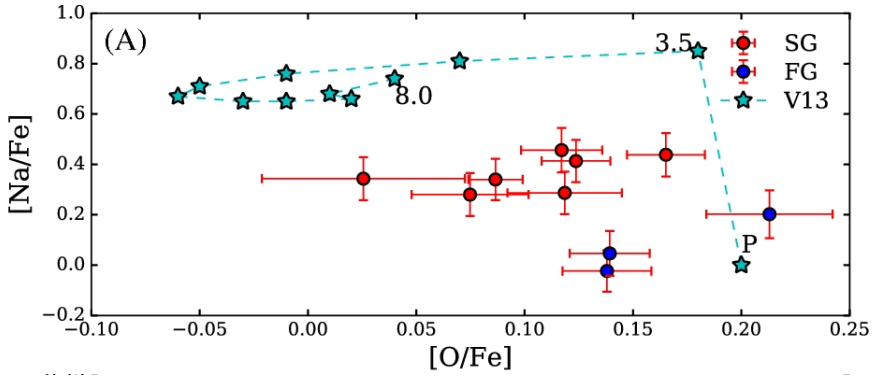

FIGURE 1.14: Na-O anti-correlation found which confirm two populations in NGC 6553 which are clearly separated in the plot. Source: Tang et al. (2017)

Additionally, APOGEE observes 'extra' targets for ancillary projects e.g Globular Clusters in the Galactic bulge and Andromeda Galaxy (M31), Medium-infrared (MIR) discovered OCs or Eclipsing Binaries among others. Some of these 'extra' targets involve totally news fields. A detailed list of the ancillary projects and its respective description

can be found on the APOGEE webpage.
Since the first data release DR10 with data from the first observation year, APOGEE has yielded great scientific contributions mainly in the stellar populations field. DR12 and DR13 are more recent releases containing data from the first three years while DR13 performed some improvements in the data processing. A new data release (DR14) is already released during the first semester of 2017 with observations from Iréné du Pont Telescope which will kick off the use of APOGEE-2S.

1.4 BACCHUS

One of the main goals of this thesis consists in a manual derivation of chemical abundances. For this purpose, we have used the Brussels Automatic Code for Characterizing High accUracy Spectra (henceforth BACCHUS) (Masseron et al., 2016) which is a semi-automatic code based on Turbospectrum (Alvarez & Plez, 1998, Plez, 2012). It can estimate stellar parameters based on a curve of growth method using iron lines. Note that this module is more efficient in the optical, but less so in NIR, since iron lines are less abundant and strong CNO molecular lines may contaminate the iron lines in NIR. Next, BACCHUS can determine chemical abundances through a line-by-line analysis. Each observed spectra line is compared with model lines of different chemical abundances using four different methods (χ^2 minimum, line-profile fitting, core line intensity and equivalent width). For more detail, see Masseron et al. (2016).
Additionally, BACCHUS is composed of three different and independent modules which derive equivalent width, stellar parameters and chemical abundances. In order to model the radiative transfer, the current BACCHUS code is based on Turbospectrum (Alvarez & Plez 1998; Plez 2012) and on MARCS atmosphere models (Gustafsson et al. 2008).

1.4.1 BACCHUS modules

As was mentioned previously, BACCHUS has three main modules which can be used in an independent way from the main directory. A brief description of each one can be found below.

- Bacchus.abund: Module to derive the chemical abundances. To use this module, the atmospheric model has to be created beforehand using the stellar parameters of the star. This module can be executed in the following way:
  ./bacchus.abund Star Element

- Bacchus.eqw: Module to derive the equivalent width when the atmospheric model is already created using the stellar parameters of the star, but it is also available to compute the micro-turbulence, convolution and metallicity for Teff and Logg known. This module can be executed in the following way[3]:
  ./bacchus.eqw Star Element

- Bacchus.param: Module to derive the stellar parameters (Teff, Logg, metallicity, micro-turbulence) from the spectrum. This module obtains the stellar parameters needed to create the atmospheric model. This module can be executed in the following way:
  ./bacchus.param Star

BACCHUS is a friendly code due its easiness to handle different aspects as the continuum fitting or line broadening. Currently, the BACCHUS code is able to work for stars of type F, G, K, M and for wavelengths from the optical to NIR. The flexibility of this code makes it a perfect alternative to realize a manual chemical analysis quickly and reliably from the APOGEE spectra.

1.5 GravPot16

Another goal of this thesis consists in the study of the cluster from the dynamic point of view. For this purpose, we have made use of the galactic kinematic software named GravPot16[4] (Férnandez-Trincado et al., in prep.).
GravPot16 is able to do the orbit calculation of Milky Way stellar bodies. This software consists of a superposition of many stellar populations belonging to the thin disk, thick disk, the stellar halo, the interstellar medium (ISM), a boxy/peanut bar, and an isothermal sphere for the dark matter component in order to obtain results as realistic as possible.
GravPot16 is based on the Besançon galaxy model in which the total gravitational potential of the Milky Way is built up self-consistently based on the approach of stellar population synthesis (see Robin et al. 2003, 2012, 2014) and Czekaj et al. (2014) keeping the classical scheme of dynamic self-consistency introduced years ago by Bienayme et al. (1987).
The software is a code that performs a variety of analyses and the typical use of GravPot16 is to compute orbital parameters and test particle simulations in an axisymmetric and/or non-axisymmetric gravitational potential, including a boxy bar through Monte Carlo simulations.

[3]For those purposes, it is recommendable use elements with strong lines such us Fe.
[4]https://fernandez-trincado.github.io/GravPot16/index.html

The input dataset to run the code consists of information about position, radial velocity, proper motions, distance and their respective errors of the object of interest.
For these purposes, large surveys which provide it is vitally importance large surveys which provide us dynamic information such us RAdial Velocity Experiment (RAVE) or the GAIA mission with data about the parallax and proper motions for up to 2 million stars which are able from Tycho-Gaia Astrometric Solution (TGAS) catalog which are just a few of those surveys with astrometric information allowing us know the motion of the stars through the Milky Way.
In this way, this thesis will try to give a comprehensive view of the selected OC, taking into account both kinematics – using GravPot16 to compute the orbital configuration of the cluster – and chemistry – using the APOGEE spectra to do a manual chemical analysis utilizing the BACCHUS code.

Chapter 2

IC 166

Now, will be introduced the object about which we will focus our efforts. IC 166 (see Fig. 2.1) has not been an OC studied in depth probably due to both it is strongly affected by the extinction in the optical range and lack of data in the IR band.

IC 166 ($l = 130.071°$, $b = -0.189°$) is an intermediate-age OC ($\sim$1.0 Gyr, Subramaniam & Bhatt (2007), Vallenari et al. (2000)) located in the outer part of the disk ($R_{GC}\approx$12 kpc). Previous literature studies of this cluster used mainly photometric data or low-resolution spectroscopic data. Using the photometric data, Burkhead (1969), Subramaniam & Bhatt (2007), Vallenari et al. (2000) estimated its age, extinction and distance; Dias et al. (2002, 2014), Loktin & Beshenov (2003), Twarog et al. (1997) gave its proper motion. With the low-resolution spectroscopic data, the radial velocity and metallicity of IC 166 are estimated in Friel & Janes (1993), Friel et al. (1989). Compared with the previous works, our study will be the first one that provides an extensive study of its chemical abundances and dynamics.

IC 166 is an intermediate-age OC, and it is buried deeply in the Galactic disk. These type of OCs are of great scientific importance (Donati et al., 2014, Friel et al., 2014, Magrini et al., 2015, Tang et al., 2017). The intermediate-age and old OCs ($\geq$1.0 Gyr) are rare by nature, because most OCs are influenced by effects such as (1) evaporation, where some members reach the escape velocity after stellar encounters with other members, or (2) close encounter with interstellar cloud. Its interaction with the giant molecular clouds along its orbit in the galactic disk has a high probability to disrupt the cluster(Gieles et al., 2006, Lamers & Gieles, 2006, Lamers et al., 2005). These effects can lead to the dissolution of the cluster in $\sim 10^8$ years (Friel, 2013). As these effects can be less severe in the outer disk, intermediate-age OCs have a high chance of survival, and thus they give us a great opportunity to study chemically and dynamically this part of the Galaxy. Moreover, IC 166 is located closely to the region (between 10 kpc and 12 kpc to the galactic center) where a break in the metallicity gradient is suggested (Cunha

et al., 2016, Frinchaboy et al., 2013, Magrini et al., 2009). An accurate determination of the cluster's distance and metallicity can be useful to constrain the nature of this break. In the next sections we will present background for this cluster realized in other works and its properties.

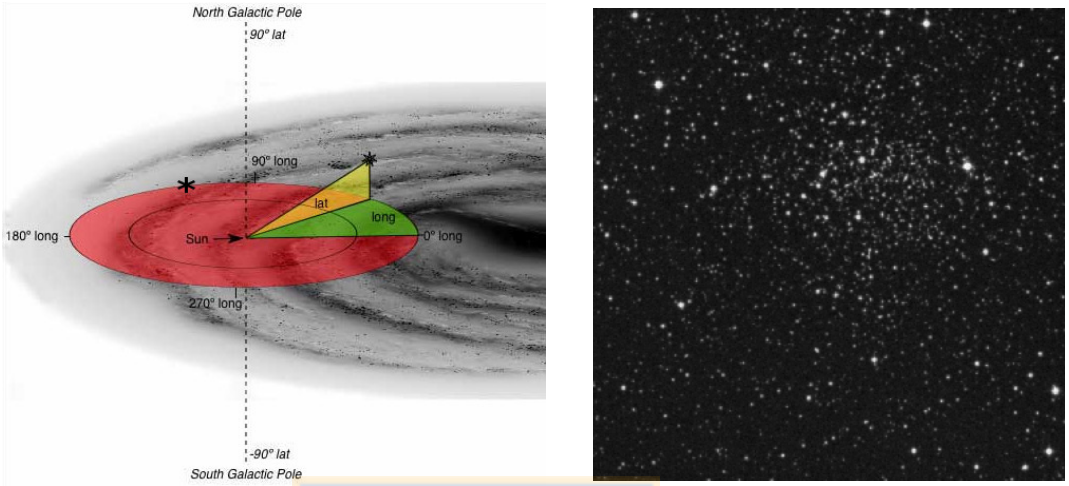

FIGURE 2.1: Left: Scheme of the MW with galactic coordinates (l and b) overploted. The black star shows the IC 166 position. Right: Picture of IC 166. Source: Peter Wienerroither

2.1 Basic Parameters of IC 166

As can be seen in the previous paragraphs, there are just a bare and not deep studies history for this cluster. On the other hand, the difference in several results in the literature requires a new analysis of this cluster using different spectra as will be done in this work.In the Table 2.1 are summarized some basic parameters of IC 166 collected in different works. Some of them reflect the discrepant results in the literature for these cluster which makes it more relevant this work.

Cluster	RA_{J2000}	DEC_{J2000}	l	b	Trumpler	Age[4]
	hh mm ss	deg	deg	deg	Class	Gyr
IC 166	01 52 30.8	+61 35 47.5	130.071	-0.189	II 1 r	1.0

Cluster	[Fe/H][1]	[Fe/H][2]	Vr[3]	E(B-V)[4]	E(B-V)[5]	Core[6]	Tidal[6]
	dex	dex	kms^{-1}	mag	mag	pc	pc
IC 166	-0.17	-0.41	-36±7	0.5±0.2	0.8±0.02	5.50	35.19

TABLE 2.1: IC 166 basic parameter found in the literature. [1]WEBDA, [2]Friel & Janes (1993), [3]Friel et al. (1989), [4]Vallenari et al. (2000), [5]Subramaniam & Bhatt (2007), [6]Kharchenko et al. (2012). Source: Own elaboration

Chapter 3

Method

3.1 Objectives

One of the objectives of this thesis work is compare directly the chemical abundance obtained from a manual abundance analysis line-by-line of the APOGEE's spectra (using BACCHUS code) with those derived automatically by ASPCAP pipeline which despite to be very accuracy, in some cases problems have been reported with its results. On the other hand, we want to provide new results for this intermediate-age OC and put it in the galactic context in order to contribute in the knowledge of the both chemical evolution and chemical patterns in the galactic disk.
Those objectives will be reached using the observed spectra by APOGEE-2N through its fourteenth data release (DR14).
In this chapter the method used will be described detailedly. The first section is focused in the membership selection and the second section is focused in the manual derivation of the chemical abundances which will be compared with ASPCAP abundances.

3.2 Looking for Cluster Members

Because APOGEE observe big sky regions and due to the strong contamination of the field stars in the galactic disk, a series of selection criteria is required for IC 166 in order to make the target selection more reliable, utilizing as many parameters as possible such as, spatial distribution, radial velocity, iron abundance, CMD location and proper motions of every star candidate.
You should note stars that approved these criteria were represented with red filled circles, while stars considered like field stars were represented with black filled circles. A detailed explanation of each criteria will be described below.

3.2.1 Spatial Distribution

The first selection criterion was the spatial location of the candidate stars. We searched, in the APOGEE database, stars that were inside, at least, of the tidal radii which is the maximum distance that one star can be under the potential of the cluster, so we can say that while the stars are closer to cluster center, there is a higher probability of belonging to the cluster than the field.

The Fig. 3.1 shows the stars observed by the APOGEE-2N survey in the field of IC 166, where potential members and fields stars were represented in red and black dots, respectively. We also plot the core radius (CR) (blue dashed line) and the tidal radius (TR) (green dashed line) obtained by Kharchenko et al. (2012). It is clear that all the potential members are inside of the TR (35.19 $\pm$ 6.10 pc) and some of them are even inside of the CR (5.50 $\pm$ 0.95 pc). Stars outside of the tidal radii were immediately discarded like stars candidate. On the other hand, there are 32 stars inside of the tidal radii, where red filled circles are the thirteen star candidates, all of them are inside of the tidal radius (blue dashed line), actually, most of them are inside of the core radius (green dashed line). While black filled circles do not satisfy the others criteria and are probably field stars.

Even though a star closer to the cluster center has a higher probability of belonging to

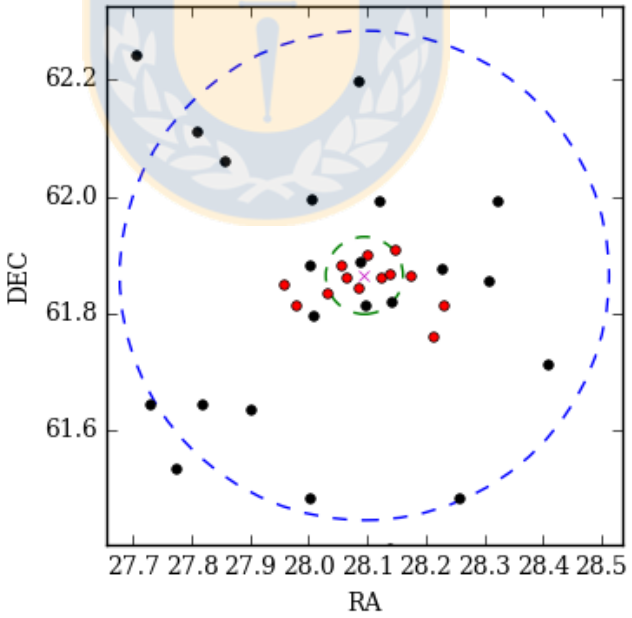

FIGURE 3.1: Spatial distribution of the APOGEE's stars (field 5060). Candidates and field stars are represented with red and black filled circles respectively. While blue and green dashed lines represent the tidal and core radii obtained by Kharchenko et al. (2012). Source: Own elaboration

the cluster than one star is in its outer part, this may be just a coincidence, since we may be seeing a field star right on the line of sight of IC 166. For this reason, more criteria

are needed to determine the membership of the cluster.
In the next sections will present kinematic and chemical criteria in order to do more robust the member selection.

3.2.2 Metallicity

As we have explained before, members stars should share a similar chemical composition. For these reason, we have used as a first approach to the chemical homogeneity expected in open clusters the [Fe/H] values measured by ASPCAP. According with those results, metallicity of IC 166 is -0.06±0.02 dex. The star-by-star metallicity found by ASPCAP for our potential members is listed in the Table 3.1.

3.2.3 Radial Velocity and Distances to the Center of the Cluster

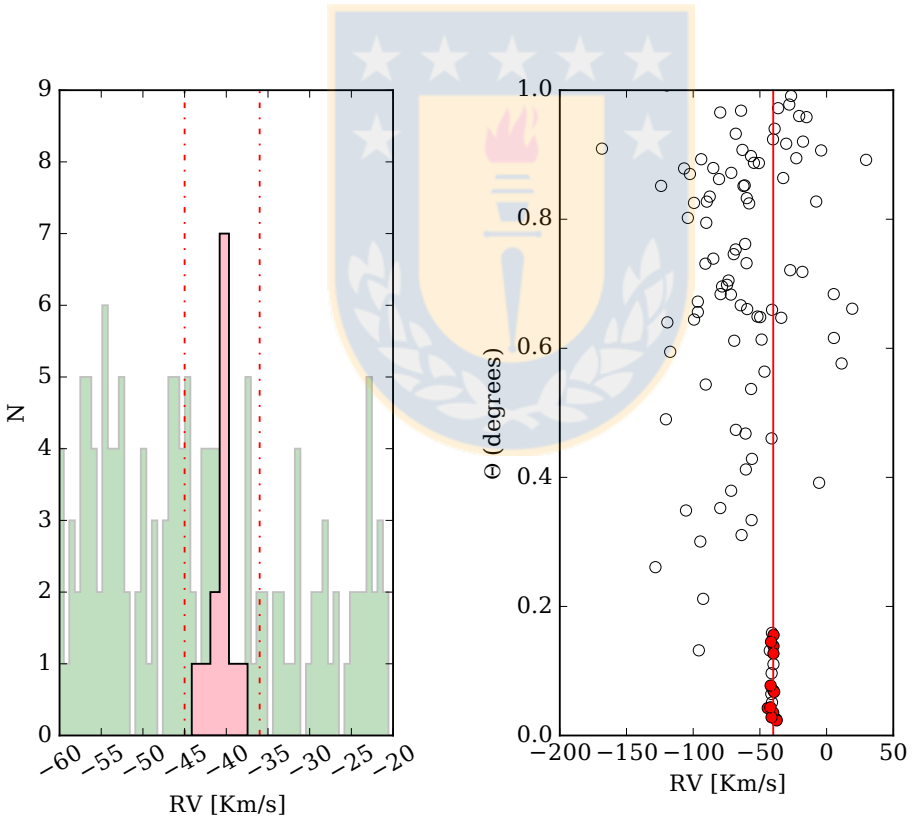

FIGURE 3.2: **Left panel:** Histogram of the radial velocity distribution of the potential cluster members. Green and pink solid bars represent the radial velocity distribution of field and cluster candidates members, respectively, while red solid line shows $\pm 3\sigma$ limit of the candidate member distribution. Source: Own elaboration **Right panel:** Distance of the stars to the cluster center (Θ) versus RV. Candidate members of IC 166 are shown as red dots and field stars of the APOGEE observation plate which includes IC 166 are empty circles. The solid red line represents the mean radial velocity of the candidate members. Source: Own elaboration

In the left panel of Figure 3.2, the RV distribution of the potential members (pink solid bar) and field stars (green solid bar) in the APOGEE observation plate that includes IC 166 are represented as histograms. Although the RV distribution is heavily contaminated by field stars, the right panel of Figure 3.2 shows that there are a lot of stars sharing a similar RV, and that our potential members are located closer to the center of the cluster (Θ) than most of the field stars. For these 13 potential members, the mean RV $= -40.58 \pm 1.66$ km s^{-1}. This value is slightly smaller than the mean found by Friel et al. (1989), -36 ± 7 km s^{-1}.

3.2.4 CMD Location

The Figure 3.3 shows the CMD of IC 166 in near-infrared filters (J and K bands) from 2MASS photometry, where red dots are our candidate members, the same description that the Figure 3.1, the small black dots and big black dots represent stars inside of the TR and inside of the CR, respectively. Although the CMD is highly contaminated by

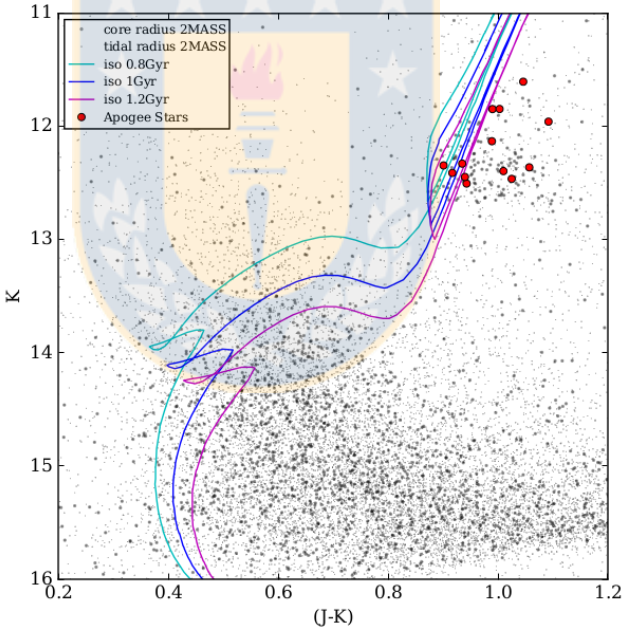

FIGURE 3.3: CMD of IC 166 using J and K filters. Small and big gray points represent stars inside of the tidal radius and the core radius observed by 2MASS, respectively. Red dots represent our potential members observed by APOGEE. Isochrones for 0.8 Gyr (sky-blue line), 1.0 Gyr (blue line) and 1.2 Gyr (green line) from PARSEC are also plotted. Source: Own elaboration

field stars, and differential reddening effects are important, it is clear that the potential members belong to the red clump of IC166. Interestingly, Vallenari et al. (2000) also reported a clear RC in IC 166, but did not find evidence of RGB stars. This is to be expected for a cluster with an age of ∼1.0 Gyr. In the same figure, we over-plotted the

theoretical isochrones from PARSEC (Bressan et al., 2012) with ages of 0.8, 1.0 and 1.2 Gyr. As the infrared CMD does not show clearly the main sequence, we plotted the same isochrones in the optical CMD.

3.2.5 Proper Motions

We have used the proper motion data from the Sampedro Catalog (Sampedro et al., 2017), which have used 3 different methods to determine the membership of 1876 OCs using UCAC4 (Zacharias et al., 2013) data. In Figure 3.4, the results obtained by Sampedro et al. (2017) for IC 166. Some of our potential members have been cataloged as cluster members by them using their different methods (M1: 6 stars, M2: 8 stars and M3: 6 stars). Those proper motion will be used latter to do the orbital configuration of the cluster (more detail in the Subsection 4.1.5).
On the other hand, Dias et al. (2014) have done a similar analysis of the proper motion of IC 166. They assigned probabilities of belonging to every stars observed. Regrettably, we only have proper motion data for 7 of our candidate stars. Membership probabilities are are listed in the last column of the Table 3.1.

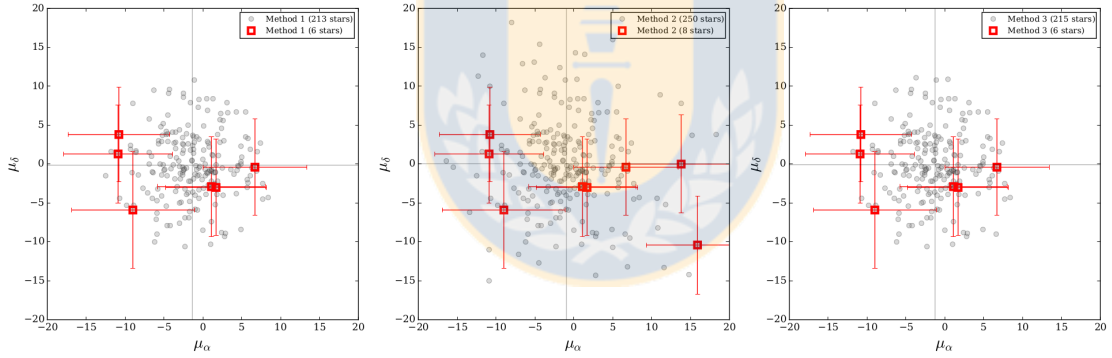

FIGURE 3.4: Proper motions of IC 166 taken from Sampedro catalog (Sampedro et al., 2017) of their 3 different methods (M1: blue dots, M2: black dots and M3: red dots). Members in common with our targets are represented with green squares. Solid lines show the respective mean proper motions of each method. Source: Own elaboration

Table 3.1 shows the basic parameters of the 13 cluster candidate members of IC 166 that we select.

3.3 Stellar Parameters

As mentioned before, the members of OCs are generally chemically homogeneous, at least to the 0.02 dex level, which is much less than our internal error. Therefore, we can use

TABLE 3.1: Summary table of potential members of IC 166. '—' symbols indicate that this star does not have proper motions measured in Dias et al. (2014). Source: Own elaboration

Apogee ID	Tag	RA[1]	DEC[1]	J[1]	K[1]	Vr[1]	[Fe/H][1]	%[2]
2M01514975+6150556	Star #1	27.957296	61.848778	13.417	12.360	-39.82	-0.05	—
2M01515473+6148552	Star #2	27.978044	61.815334	13.403	12.393	-39.83	-0.08	95
2M01520770+6150058	Star #3	28.032106	61.834946	13.446	12.503	-39.95	-0.09	96
2M01521347+6152558	Star #4	28.056156	61.882183	13.487	12.462	-44.14	-0.05	—
2M01521509+6151407	Star #5	28.062883	61.861309	13.118	12.129	-40.17	-0.05	84
2M01522060+6150364	Star #6	28.085842	61.843445	12.835	11.845	-37.45	-0.03	95
2M01522357+6154011	Star #7	28.098241	61.900307	13.262	12.327	-40.03	-0.09	96
2M01522953+6151427	Star #8	28.123055	61.861885	12.649	11.603	-41.27	-0.04	—*
2M01523324+6152050	Star #9	28.138523	61.868073	13.244	12.343	-42.17	-0.05	63
2M01523513+6154318	Star #10	28.146393	61.908844	13.326	12.409	-39.29	-0.08	—
2M01524136+6151507	Star #11	28.172348	61.864094	13.385	12.445	-41.97	-0.05	93
2M01525074+6145411	Star #12	28.211422	61.76144	13.048	11.956	-39.74	-0.09	—
2M01525543+6148504	Star #13	28.230962	61.814007	12.847	11.844	-41.68	-0.07	—*

[1] Data from ASPCAP
[2] Membership probability from Dias et al. (2014)

OC stars to calibrate the chemical abundances derived by ASPCAP. Before measuring the chemical abundances manually, we need to determine the stellar parameters first, because they are closely related to each other. Here we use two atmospheric models, MARCS (Gustafsson et al., 2008) and KURUCZ (Kurucz, 1970), where they assume a plane parallel and a spherical atmospheric geometry, respectively.

- We run the FERRE code (Allende Prieto et al., 2006) to search for the χ^2 minimum between the observed spectrum and the MARCS model spectra. The stellar parameters of the observed spectrum are interpolated from the nearest neighbors in the model parameter space. The results are shown in the second, third and fourth columns of Table 3.2.

- Besides the ASPCAP chemical abundances, DR14 also gives chemical abundances using the data-driven software, *The CANNON* (Ness et al., 2015). The training set of *The CANNON* is the stellar parameters derived by ASPCAP for high-quality stars, where KURUCZ model atmospheres are assumed in ASPCAP. *The CANNON*-derived stellar parameters are given in the sixth, seventh and eighth columns of Table 3.2.

Figure 3.5 shows stellar parameters obtained from *The CANNON* (black dots), FERRE (pink dots) and ASPCAP (red dots). PARSEC (Bressan et al., 2012) isochrones with ages of 0.8 (cyan line), 1.0 (blue line) and 1.2 Gyr (green line) are over-plotted. We find that (1) the stellar parameters obtained by *The CANNON* fit the isochrones best; (2) the stellar parameters obtained from ASPCAP have a offset in Teff with respect to the isochrone Teff; (3) FERRE stellar parameters are shifted to greater Logg and

to greater Teff with respect to the theoretical isochrones. We adopt *The CANNON* and FERRE stellar parameters for our analysis, in order to estimate the uncertainties of chemical abundances introduced by adopting different sets of stellar parameters. Finally, the micro-turbulence is computed using BACCHUS.

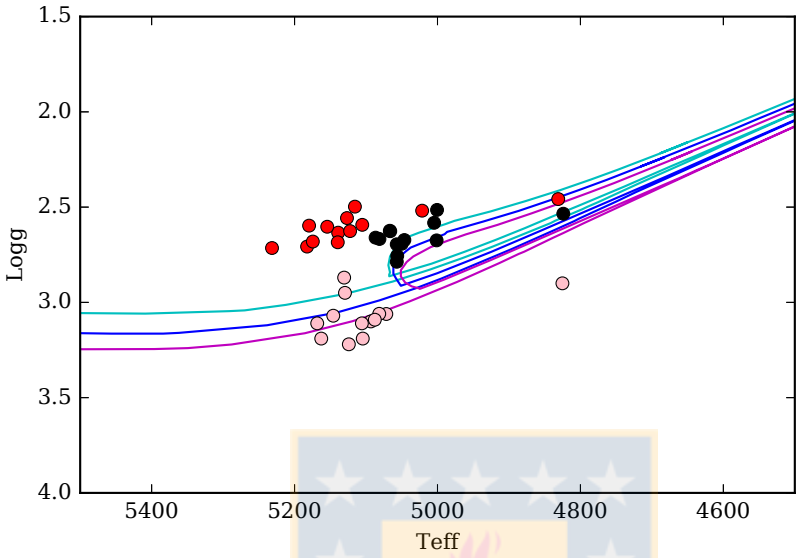

FIGURE 3.5: Teff-Logg plane: Stellar parameter obtained using MARCS and KURUCZ models are represented with red and black dots, respectively. Isochrones for 0.8 (sky-blue line), 1.0 (blue line) and 1.2 Gyr (green line) from PARSEC are also plotted. Source: Own elaboration

TABLE 3.2: Stellar parameters obtained from CANNON and FERRE codes. Source: Own elaboration

	FERRE				CANNON			
ID	Teff	Logg	[Fe/H]	v^{*}_{micro}	Teff	Logg	[Fe/H]	v^{*}_{micro}
star #1	5070.00	3.05	-0.01	1.50	5050.00	2.70	-0.06	2.05
star #2	5080.00	3.05	-0.08	1.30	5045.00	2.70	-0.10	1.40
star #3	5130.00	2.95	-0.05	1.30	5000.00	2.70	-0.20	1.50
star #4	5090.00	3.10	-0.05	1.45	5055.00	2.75	-0.08	1.60
star #5	5145.00	3.10	-0.04	1.20	5065.00	2.60	-0.05	1.90
star #6	5105.00	3.20	-0.05	1.30	5085.00	2.65	-0.09	1.85
star #7	5170.00	3.10	-0.10	1.35	5080.00	2.65	-0.13	2.00
star #8	4825.00	2.90	-0.07	0.65	4825.00	2.50	-0.02	1.90
star #9	5105.00	3.10	-0.11	1.80	5065.00	2.60	-0.13	2.30
star #10	5160.00	3.20	-0.10	0.55	5055.00	2.70	-0.13	1.50
star #11	5125.00	3.20	-0.06	1.05	5055.00	2.80	-0.10	1.60
star #12	5130.00	2.90	-0.06	1.60	5000.00	2.50	-0.09	1.90
star #13	5090.00	3.10	-0.05	1.10	5005.00	2.60	-0.06	2.05

* Values measured by BACCHUS.

3.4 Chemical Abundances Derivations

In this paper, we try to provide a comparison between the automatic chemical abundances derived by the APOGEE pipeline ASPCAP and the manually derived chemical abundances using the Brussels Automatic Code for Characterizing High accUracy Spectra (henceforth BACCHUS) (Masseron et al., 2016) which is a semi-automatic code based on Turbospectrum (Alvarez & Plez, 1998, Plez, 2012). It can estimate stellar parameters based on a curve of growth method using iron lines. Note that this module is more efficient in the optical, but less so in the near-infrared (NIR), since iron lines are less abundant and strong CNO molecular lines may contaminate the iron lines in the NIR. Next, BACCHUS can determine chemical abundances through a line-by-line analysis. Each observed spectral line is compared with model lines of different chemical abundances using four different methods (χ^2 minimum, line-profile fitting, core line intensity and equivalent width). For more detail, see Masseron et al. (2016).

On the other hand, due to the large amount of data in the APOGEE survey, the APOGEE community have developed the APOGEE Stellar Parameter and Chemical Abundances Pipeline (ASPCAP; more detail in García Pérez et al. (2016)) to derive the stellar parameters and chemical abundances automatically. First, ASPCAP searches the χ^2 minimum between the observed spectrum and the atmospheric model spectra. The stellar parameters of the observed spectrum are interpolated from the nearest neighbors in the model parameter space. The parameter space of the atmospheric models include not only effective temperature, surface gravity, microturbulent velocity and metallicity, but also C, N, O and α-element abundances, because the strong molecular absorption (CO, OH, CN) lines in the NIR can significantly change the continuum level. After obtaining the stellar parameters, ASPCAP measures the chemical abundances using spectral windows for individual elements.

We derive chemical abundances of our sample stars using BACCHUS as follows: 1) First, we need to estimate stellar parameters of our sample stars. As we mention above, estimating stellar parameters based on a curve of growth method is not appropriate for NIR spectra. Besides, since IC 166 is strongly affected by extinction (E(B-V)$\approx$ 0.65), the stellar parameters computed from photometry are plagued by large uncertainties. As an alternative, we use stellar parameters (Teff, Logg and [Fe/H]) obtained by *The CANNON* and FERRE codes. 2) Next, we use BACCHUS to estimate the line broadening caused by microturbulence and also the instrumental broadening. 3) Finally, we run BACCHUS to determine chemical abundances of each element line-by line. Though the code can detect significant bad fits, like a sudden drop in the flux due to malfunction of the detector, the code may over-fit the spectra even if the SNR is too low. To make our abundances more reliable, we check each fitting line-by-line. We first reject the weak lines where the signal is too weak. Among the stronger lines, we selected those

where the four different methods in BACCHUS are able to measure them. After that, we do a visual inspection on the selected lines. Bad fits between observed lines and model lines are rejected. The abundance of a given element is the mean of the abundances of all lines determined by the χ^2 method, which is more robust. Standard deviations are treated as errors. On the other hand, we note that even though we did not measure the abundances of Oxygen, Carbon and Nitrogen (from the molecules of OH, CO and CN, respectively), the continuum of our spectra could be adjusted adequately so unlike (Hawkins et al., 2016, Souto et al., 2016), we directly measure the atomic abundances. While ASPCAP gives chemical abundances from more than 20 molecular and atomic species, the chemical abundances suffer from different uncertainties related to the strength of the element lines (Holtzman et al., 2015). Our manual analysis with BACCHUS tries to improve the credibility of the derived chemical abundances by using only stronger lines. We derive abundances of Mg I, Si I, Ca I and Ti I (α-elements); Al I and K I (Light odd-elements); and Mn I and Fe I (iron-peak elements). Our abundances were scaled relative to the solar abundances (Asplund et al., 2005), which is consistent with ASPCAP.

3.5 Orbit Computation of IC 166

To get a comprehensive view of IC 166, we further investigate the dynamics of this cluster in this section. We use the Galactic dynamic software named GravPot16 (J.G. Férnandez-Trincado et al., in preparation). GravPot16 considers a potential as realistic as possible, taking into account a stellar component (from the thin and thick disk and also a stellar halo), dust and gas (forming the interstellar medium), a peanut/boxy bar and also a uniform spherical dark matter distribution.

Since we have in common only some of our sample stars with UCAC-4, this sample may be too small to represent the proper motion of IC 166 stars. In order to increase our sample size, we select stars from Sampedro Catalog (Sampedro et al., 2017). They have used three different methods to determine the membership of 1876 OCs using UCAC-4 data. In the case of IC 166, they have identified more than 200 stars which belong to the cluster. We have used the mean proper motions obtained by them for those three different methods (henceforth M1, M2, M3). On the other hand, RVs and positions are taken from APOGEE DR14, while the heliocentric distance was taken from Dias et al. (2002). The results of this analysis can be found in the Subsection 4.1.5.

Chapter 4

Results

In the present chapter will be shown the chemical and dynamic results. It will be separated in two main parts. In the first one, will be presented manual chemical results after using BACCHUS with two different stellar parameters (CANNON and FERRE). Also a comparison between them will be analyzed and finally a estimation of their respective error is shown. On the other hand, in the second part of these chapter, the results from the dynamic will be shown after use the software GravPot16 which computed the orbit configuration of IC166 using kinematic data from Sampedro catalog (Sampedro et al., 2017). Both sections will be described in more detail below.

4.1 Manual chemical results

Here are presented the results from both stellar parameter obtained from CANNON, which use KURUCZ model, and FERRE, which use MARCS model. In the table can be found the elemental line by line abundance for every member stars, while its counterpart can be found in the table. In those tables the lines that can be found in the APOGEE spectra are shown. Lines which are noise dominated, blended effect or too weak will be denoted with '—' symbol, thus just abundances from stronger lines are shown in order to get more precise and confident results. The selected elements (Fe, Mg, K, Si, Ti, Ca, Mn) include light, iron peak and α-elements.

4.1.1 Chemical abundances from BACCHUS vs. ASPCAP

As mentioned above , we manually derived chemical abundances for our sample stars using BACCHUS, where two different sets of stellar parameters from FERRE and *The CANNON* are assumed. Line-by-line measurements are presented for each member of

the cluster in tables which can be found in the end of this chapter. While the latter table shows the results using FERRE stellar parameters, Table 4.3 was obtained considering *The CANNON* stellar parameters. Each line center (in air wavelength) is listed in the second column of Table 4.3. Both abundance A(X) and the solar scaled abundance are shown after each element. The '—' symbol is used to indicate that it was not possible to measure the line by the four different methods available in BACCHUS, due to effects such as: saturation, weak line, noise or blending.

Fe, Mg and Si are the elements with both the strongest and more numerous lines in the spectra with 9, 3 and 14 lines, respectively. We remind the reader that even a strong line could be rejected if it could not be measured by the four different methods. On the other hand, for Titanium and Potassium, we can only identify one line in only a few stars. Therefore, the Ti and K abundances should be used with caution.

Figure 4.1 shows the abundances obtained by BACCHUS (Mg, Si, Ca, Ti, Al, K, Mn and Fe) using two different sets of stellar parameters. They were also compared with ASPCAP results which were published in APOGEE DR14.

- Al: $[\mathrm{Al/Fe}]_{CANNON}$ are in good agreement with $[\mathrm{Al/Fe}]_{FERRE}$. They also have similar dispersion, 0.04 dex. On the other hand, the large dispersion that ASPCAP measured for Al (0.35 dex) is not consistent with the homogeneity expected in OCs. This may be related to the fact that ASPCAP derives abundances using all the spectral lines, even for weak Al lines (15956.675 Å, 15968.287 Å) and a saturated Al line (16763.359 Å).

- K: $[\mathrm{K/Fe}]_{CANNON}$ are in good agreement with $[\mathrm{K/Fe}]_{FERRE}$; $[\mathrm{K/Fe}]_{CANNON}$ and $[\mathrm{K/Fe}]_{FERRE}$ are systematically higher compared to $[\mathrm{K/Fe}]_{ASPCAP}$, and the difference is smaller for $[\mathrm{K/Fe}]_{FERRE}$. Because we can measure only one line for K in most of the stars, the results about K should be taken with caution.

- Fe: $[\mathrm{Fe/H}]_{CANNON}$ and $[\mathrm{Fe/H}]_{FERRE}$ are systematically smaller and more scattered than $[\mathrm{Fe/H}]_{ASPCAP}$. We found $[\mathrm{Fe/H}]_{CANNON} = -0.15 \pm 0.05$ dex and $[\mathrm{Fe/H}]_{FERRE} = -0.10 \pm 0.06$ dex, which are slightly less than the ASPCAP mean used as input by BACCHUS. These mean Iron abundances are consistent with the value found by Twarog et al. (1997).

- Mg: $[\mathrm{Mg/Fe}]_{CANNON}$ and $[\mathrm{Mg/Fe}]_{FERRE}$ are systematically smaller compared to $[\mathrm{Mg/Fe}]_{ASPCAP}$. But $[\mathrm{Mg/Fe}]_{CANNON}$ and $[\mathrm{Mg/Fe}]_{FERRE}$ show a comparable dispersion compared to $[\mathrm{Mg/Fe}]_{ASPCAP}$. It is interesting to note that stars #3 (red dot) and #12 (sky-blue dot) show more scattered $[\mathrm{Mg/Fe}]_{ASPCAP}$.

TABLE 4.1: Mean chemical abundances measured by BACCHUS using stellar parameters from CANNON and FERRE for thirteen potential members. Source: Own elaboration

Element	Bacchus$_{cannon}$	Bacchus$_{ferre}$	ASPCAP
Mg	-0.04±0.05	-0.16±0.04	0.02±0.04
Si	0.10±0.04	0.09±0.04	0.07±0.06
Ca	-0.02±0.03	-0.07±0.03	0.00±0.04
Ti	-0.03±0.02	-0.04±0.03	-0.01±0.07
Al	0.18±0.04	0.14±0.04	0.03±0.35
K	0.04±0.07	0.02±0.08	-0.03±0.07
Mn	0.01±0.03	0.00±0.03	0.00±0.03
Fe	-0.15±0.05	-0.10±0.06	-0.06±0.02

- Si: In the case of Silicon, the resulting abundances derived from three different methods are similar, thus the comparison of each pair follows the one-to-one line. Similar to the case of Magnesium, [Si/Fe]$_{ASPCAP}$ show larger scatter, and stars #3 and #12 also have more scattered [Si/Fe]$_{ASPCAP}$.

- Ca: [Ca/Fe]$_{CANNON}$ and [Ca/Fe]$_{FERRE}$ generally agree with [Ca/Fe]$_{ASPCAP}$, though [Ca/Fe]$_{FERRE}$ may be slightly smaller.

- Ti: [Ti/Fe]$_{CANNON}$ and [Ti/Fe]$_{FERRE}$ generally agree with [Ti/Fe]$_{ASPCAP}$, though we caution that only one line can be measured in some stars.

- Mn: [Mn/Fe]$_{CANNON}$ and [Mn/Fe]$_{FERRE}$ agree with [Mn/Fe]$_{ASPCAP}$. All of them have abundances close to solar.

The abundances and their respective standard deviations in each element measured by BACCHUS, using both stellar parameters, can be seen in Table 4.1. In general, [X/Fe]$_{CANNON}$ is larger than [X/Fe]$_{FERRE}$. However, they mostly agree within the uncertainties, except Mg and Ca. These two elements are more sensitive to the change of stellar parameters.

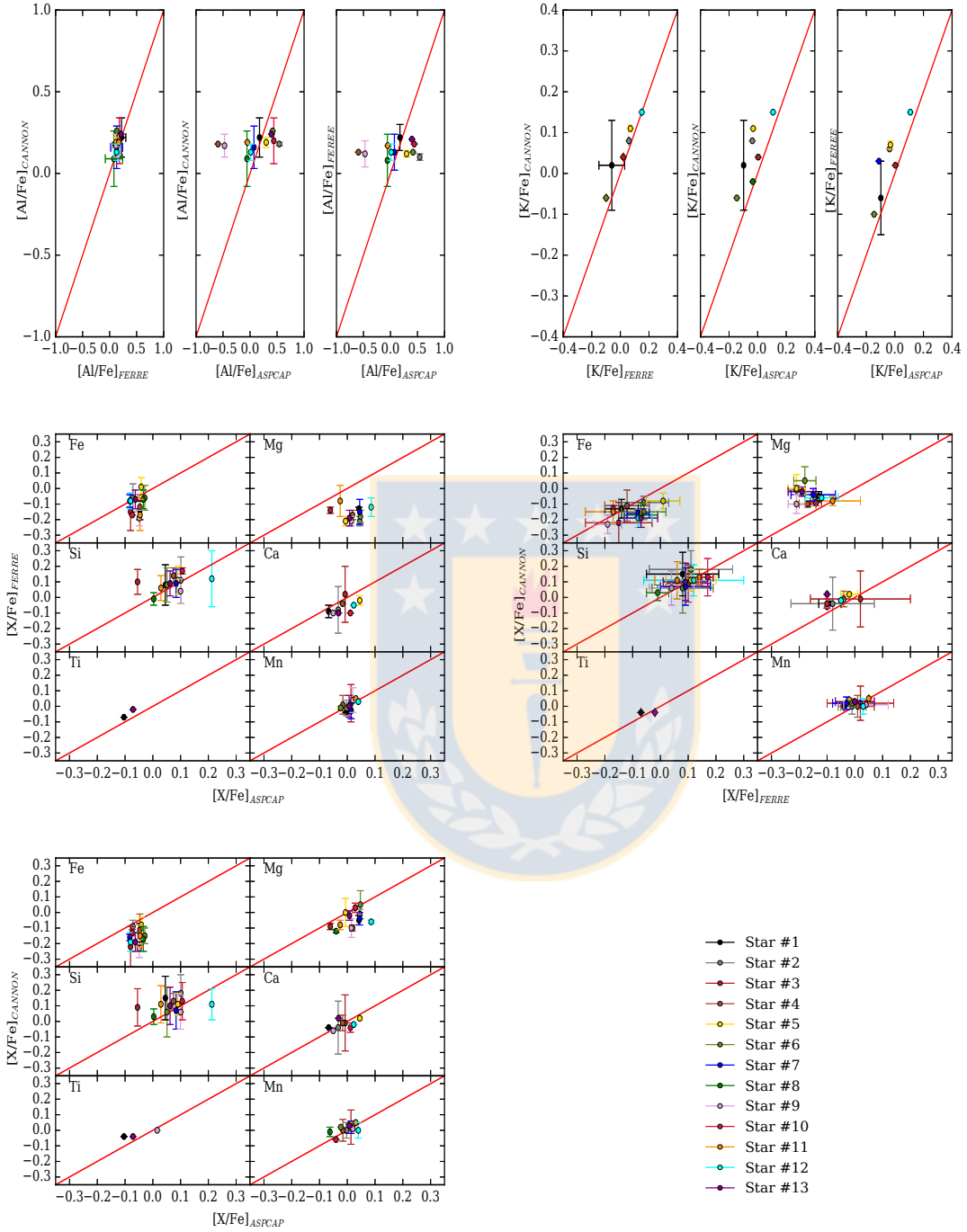

FIGURE 4.1: Comparisons between the resulting abundances of Mg, Si, Ca, Ti, Al, K, Mn and Fe using two different sets of stellar parameters obtained by CANNON and FERRE. They are also compared with ASPCAP results which were published by APOGEE DR14. The red solid line represent a one-to-one line and, on the right lower panel, the different colors of the dots indicate a specific member star. Source: Own elaboration

4.1.2 Comparison with the literature

Many studies have attempted to trace and understand the formation history and chemical evolution of the thin and thick disks, bulge and halo (Battistini & Bensby, 2015, Bensby et al., 2014, Chen et al., 2000), and they have been joined by the homogeneous and large data sets such as APOGEE (Majewski et al., 2017), GAIA-ESO (Gilmore et al., 2012, Randich et al., 2013), GALAH (De Silva et al., 2015).

To compare with our results, we have assembled (1) a sample of dwarf stars in the solar neighborhood using optical filters from Bensby et al. (2014) (gray crosses in Mg, Ca, Si, Ti and Al panels); (2) a sample of dwarf stars in the solar neighborhood from Battistini & Bensby (2015) (gray crosses in the Mn panel); (3) a sample of F and G main-sequence stars of the disk taken from Chen et al. (2000) (gray crosses in the K panel) and (4) the APOKASC sample which were re-analyzed using BACCHUS by Hawkins et al. (2016) (cyan crosses in Mg, Si, Ti, Ca, K, Al and Mn panels). Finally, we show the ASPCAP abundances with yellow triangles, and our results using stellar parameters from CANNON and FERRE are represented with magenta and blue triangles, respectively.

- α-elements: Magnesium, Silicon, Titanium and Calcium are generally considered as α-elements, because they are formed by the fusion of α-particles. These elements can be produced in large quantity by Type II Supernovae (Samland, 1998). The abundances of the α-elements decrease while the metallicity increases after the onset of Type Ia SNe, (e.g., Bensby et al. 2014 and Hawkins et al. 2016). If we look closely, this trend is separated into two sequences, especially for Mg. Using the APOGEE data, Hayden et al. (2015) found that the higher [α/Fe], more metal-poor sequence is dominated by thick disk stars, while the lower [α/Fe], more metal-rich sequence is dominated by thin disk stars. In general, our results follow the pattern formed by field stars at the metallicity of IC 166 members. However, our values are slightly lower in Mg and Ti when we compared with Bensby et al. (2014), though still inside the uncertainty range.

- Light odd-Z elements: Potassium is primarily the result of the burning of oxygen in massive stellar explosions (Clayton, 2007), so it is related to the $\alpha-$elements formation (Zhang et al., 2006), expelled from Type II Supernovae (Samland, 1998). Aluminum is formed during the carbon burning in massive stars, mostly by the reactions between ^{26}Mg and the excess neutrons (Clayton, 2007). The Al abundances may also be changed through the MgAl cycle at extremely high temperature, e.g., inside the AGB stars(Arnould et al., 1999, Samland, 1998). Although there is not much observational data for K, the available data indicate that its abundance increases as metallicity decreases. Figure 4.2 shows that the results from Chen et al.

(2000) are shifted to higher abundances with respect to Hawkins et al. (2016), probably due to differences in the adopted solar abundances. Our results follow the expected trend for field stars at this metallicity. On the other hand, the Al abundance decreases as metallicity increases, and it stays relatively constant for metallicity greater than solar. We find a large discrepancy between literature and ASPCAP result, especially due to the very large dispersion in the latter.

- Iron-peak elements: Manganese belongs to the Iron group. Mn is thought to form in explosive silicon burning (Battistini & Bensby, 2015, Clayton, 2007, Woosley & Weaver, 1995). Manganese is produced in both Supernovae Type II and Supernovae Type Ia which create Mn in considerable amounts (Clayton, 2007). According to the observations, Mn closely follows Fe. In this sense, most of our stars are in agreement with the literature, while a few of them, especially the more metal-poor ones, have slightly higher values.

To summarize, the BACCHUS results are in good agreement with the literature. In general, $[X/Fe]_{CANNON}$ are slightly larger than $[X/Fe]_{FERRE}$. Compared to the scatters in ASPCAP abundances, $[X/Fe]_{CANNON}$ and $[X/Fe]_{FERRE}$ show similar scatter for K and Mn; smaller scatter for Si, Ca, Ti, and Al, but larger scatter for Fe and Mg. The most remarkable improvement compared to the ASPCAP results is the Al abundance, in which we find a much smaller dispersion.

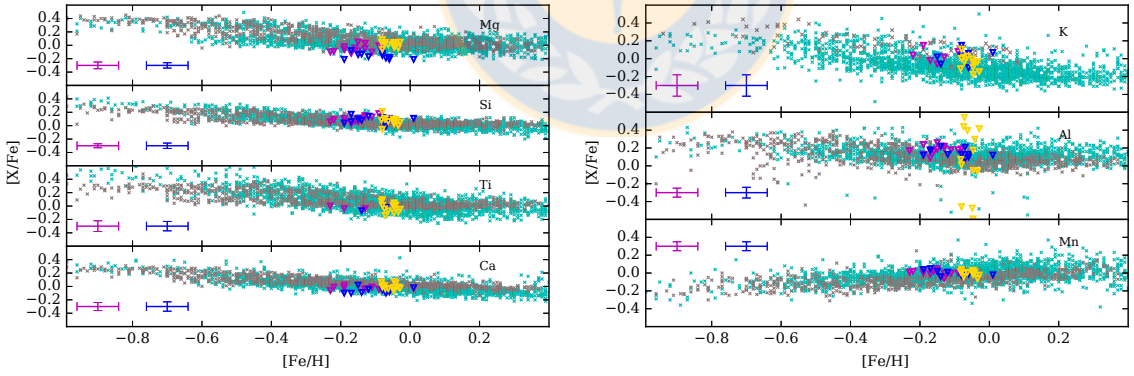

FIGURE 4.2: [X/Fe] versus [Fe/H] plane for each member of IC166. Magenta and blue triangles represent the result obtained by BACCHUS using the stellar parameters from CANNON and FERRE, respectively. They are contrasted with the literature: cyan crosses from Hawkins et al. (2016) results, while gray crosses for Ca, Ti, Mg, Si, Al come from Bensby et al. (2014), the sources of the gray crosses for K, Mn are Chen et al. (2000) and Battistini & Bensby (2015), respectively. Source: Own elaboration

4.1.3 Metallicity Gradient

There have been many different studies of the radial metallicity gradient (Cunha et al., 2016, Friel, 1995, Frinchaboy et al., 2013, Jacobson et al., 2016), trying to understand

the chemical evolution of the galactic disk. Open clusters are one of the best tracers for this propose, because they are located along the whole galactic disk and they provide relatively easily measured chemical and kinematic properties. In spite a large number of studies, agreement has not been reached on the slope of the gradient or on the location of a possible break in the metallicity trend. All studies do agree that the metallicity decreases with increasing galactic radius, at least for the older OCs.

Figure 4.3 shows the metallicity gradient along the galactic disk found by Frinchaboy et al. (2013). Blue, cyan and red dots represent OCs with log(age)<8.5, 8.5≤log(age)<8.5 and log(age)≥9.0, respectively. The vertical green dashed lines at 8.5 kpc and 10 kpc represent the assumed distance from the Sun to the GC and the break in metallicity gradient, respectively. Finally, the magenta and orange stars represent $[Fe/H]_{FERRE}$ and $[Fe/H]_{CANNON}$, respectively. We have used the distance to the Sun of IC 166 (4.8 kpc; Dias et al. (2002)) to be consistent with Frinchaboy et al. (2013). They linearly fit their whole sample and found a slope of -0.09 ± 0.03 dex kpc^{-1} (blue dashed line), and on the other hand, they also fitted the inner and outer disk (≥10 kpc) separately with two lines. They found slopes of -0.20 ± 0.08 dex kpc^{-1} (inner disk) and -0.02 ± 0.09 dex kpc^{-1} (outer disk), represented with red dashed lines. After we plot our manual-derived metallicity of IC 166, we find that our results basically agree with the trend given by Frinchaboy et al. (2013), considering that the metallicity scatter in the OCCAM OCs is substantial.

4.1.4 [α/Fe] versus [Fe/H]

As noted above, α-elements are formed from the reactions with α-particles (He nuclei), which are active in Type II SNe. On the other hand, Fe is generated in SN Ia (although also, in smaller amount, in SNe II), therefore [α/Fe] is related to the ratio of Type II over Type Ia SNe, which reflects their birthplace environment.

The [α/Fe] versus [Fe/H] plane shows a clear bimodality (Bensby et al., 2005, Hayden et al., 2015, Kordopatis et al., 2015, Masseron & Gilmore, 2015), where α-element abundances decrease as metallicity increases until solar metallicity. The high [α/Fe] sequence consists of mainly thick disk stars; and the low [α/Fe] sequence is flatter and it consists of thin disk stars. The two sequences reflect different chemical enrichment histories. Because the main polluters of the ISM in the early stages of galaxy formation are Type II SNe, we see high α-element at low metallicities. After $\sim$ 1 Gyr, Type Ia SNe start to emerge, generating a significant amount of iron-peak elements, and the iron-peak element fraction in the ISM increases quickly (Bensby et al., 2005). In this way, [α/Fe] decreases as metallicity increases.

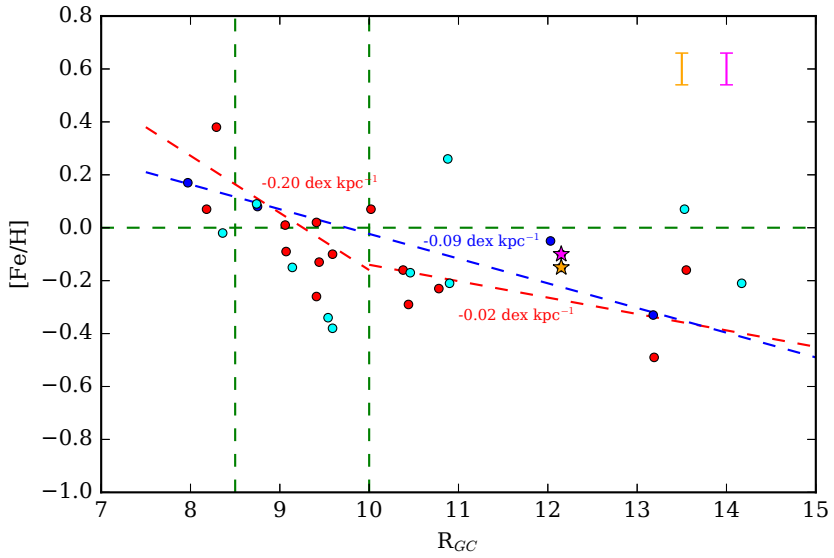

FIGURE 4.3: Gradient of metallicity along the galactic disk using open clusters as tracer. Plane of [Fe/H] versus galactocentric distance taken from Frinchaboy et al. (2013). Blue, cyan and red dots represent clusters with log(age)<8.5, 8.5≤log(age)<8.5 and log(age)≥9.0, respectively. The vertical green dashed lines at 8.5 kpc and 10 kpc represent the assumed distance from the Sun to the GC and the break of metallicity. The red and blue dashed lines are the different slopes found by Frinchaboy et al. (2013). Finally, the magenta and orange stars represent the metallicity measured by BACCHUS using the stellar parameters from FERRE and CANNON, respectively. Source: Own elaboration

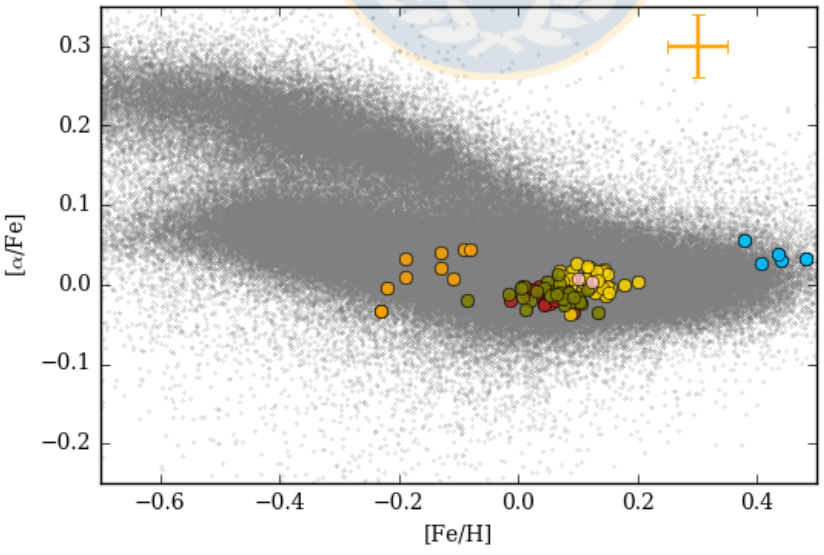

FIGURE 4.4: [α/Fe] versus [Fe/H]. Gray dots shows the high and low α-sequence formed by thick and thin disk stars observed by APOGEE DR14. Five open clusters studied by (Linden et al., 2017) (M67, NGC7789, NGC6819, NGC6791, NGC188 in green, red, yellow, blue and pink dots, respectively) are also shown. Stars of IC 166 are shown in orange. Source: Own elaboration

Figure 4.4 shows stars from APOGEE DR14 as gray dots. Five OCs (M67, NGC7789, NGC6819, NGC6791, NGC188 in green, red, yellow, blue and pink dots, respectively) studied by Linden et al. (2017) are added, and also IC 166 (orange dots). Here the IC 166 abundances are obtained by BACCHUS using the CANNON stellar parameters. We note that the α-elements taken into account in this plot are Mg, Si and Ca. All of the IC 166 stars follow the expected trend for thin disk stars, though our stars are slightly more scattered compared to other clusters.
IC 166 fits in the low α-sequence and indicates that this cluster belongs to the thin disk, at least from the chemical point of view. Its slightly lower metallicity compared to the other clusters is due to its larger Galactocentric distance and the radial gradient investigated above.

4.1.5 Dynamic results

For the Galactic model we employ the Galactic dynamic software called GravPot16[1] (Fernández-Trincado et al. 2018, in preparation), a semi-analytic, steady-state, three dimensional gravitational potential based on the mass density distributions of the Besançon Galactic model (Robin et al., 2012, 2003, 2014) observationally and dynamically constrained. The model is constituted by seven thin disk components, two thick disks, the Interstellar Medium (ISM), a Hernquist stellar halo, a rotating bar component, and surrounded by a spherical dark matter halo component, that fits fairly well the structural and dynamical parameters to the best we know of the Milky Way. A description of this model and its updated parameters appears in a score of papers (Fernández-Trincado et al., 2017, 2016)

The Galactic potential is scaled to the Sun's galactocentric distance, 8.3±0.23 kpc, and the local rotation velocity, 239±7 km s^1 (e.g., Brunthaler et al., 2011). We assumed the Sun's orbital velocity vector [$U_\odot$,$V_\odot$,$W_\odot$]=[$11.1\pm^{+0.69}_{-0.75}$, $12.24\pm^{+0.47}_{-0.47}$, $7.25\pm^{+0.37}_{-0.36}$] (Schönrich et al., 2010). A long list of studies has presented in the literature different ranges for the bar pattern speeds. For our computations, the values Ω_{bar} = 35, 40, 45 and 50 km s$-$1 kpc^{-1} are employed. These values are consistent with the recent estimate of Ω_{bar} given by (Fernández-Trincado et al. (2017), Portail et al. (2017), Monari et al. (2017a), Monari et al. (2017b)). We consider an angle of $\phi = 20°$ for the present-day orientation of the major axis of the Galactic bar and the Sun-Galactic center line. The total mass of the bar taken in this work is 1.1×10^{10} $M_\odot$, that corresponds to the dynamical

[1] `https://gravpot.utinam.cnrs.fr`

constraints towards the Milk Way bulge from massless particle simulations (Fernández-Trincado et al., 2017), which is consistent with the recent estimate given by Portail et al. (2017).

The positional information for 13 high probability stellar members of IC 166 were combined with kinematics information from the APOGEE-2 survey (which allows for precise radial velocity measurement) to estimate a probable orbit for the cluster. For the stars observed with APOGEE-2, the radial velocity was measured independently for each star (archiving a typical uncertainty of ~ 0.1 km s^{-1}). We direct the readers to Nidever et al. (2015) for a full description of the method used to measure the radial velocities in APOGEE-2 spectra. For our 13 likely cluster members, we find the strong velocity signature of the cluster (see text). For these stars we find that the systemic radial velocity of the cluster is $RV = -40.58 \pm 1.66$ km s^{-1}, which is comparable to the cluster radial velocity given by Friel et al. (1989), $= -36\pm 7$ km s^{-1}. IC 166 has been cataloged as an intermediate-age (1.0 Gyr; Subramaniam & Bhatt (2007), Vallenari et al. (2000)) stellar cluster at a heliocentric distance of 4800 kpc (Dias et al., 2002). In order to construct the orbit, we employed this distance estimate.

The proper motions were adopted from the Sampedro et al. (2017) catalog. They used three different methods to determine the membership for 1876 OCs using UCAC-4 data (Zacharias et al., 2013). According to their results, taking into account more than 200 members of IC166, the mean proper motions of IC 166 are:

$$(\mu_\alpha, \mu_\delta)^{213-stars}_{M1} = (-1.25 \pm 4.21, -0.12 \pm 4.26) masyr^{-1}$$

$$(\mu_\alpha, \mu_\delta)^{250-stars}_{M2} = (-1.08 \pm 5.80, -0.02 \pm 5.88) masyr^{-1}$$

$$(\mu_\alpha, \mu_\delta)^{215-stars}_{M3} = (-1.17 \pm 4.14, -0.06 \pm 4.52) masyr^{-1}$$

The orbit of IC 166 is computed adopting a simple Monte Carlo procedure for different bar pattern speeds as mentioned above. For each simulation, we time-integrated backwards 10^3 orbits under variations of the initial conditions (proper motions, radial velocity, heliocentric distance, Solar position, Solar motion and the velocity of the local standard of rest) according to their estimated errors, where the errors are assumed to follow a Gaussian distribution. The results of these computations are presented in Figure 4.5, Figure 4.6 and 4.7. These figures shows the probability densities of the resulting orbits projected on the meridional and equatorial Galactic planes in the non-inertial reference frame where the bar is at rest. The yellow and red colors correspond to more probable regions of the space, which are crossed more frequently by the simulated orbits. The final point of each of these orbits has very similar position to the current one of IC 166; For all those Figures, we have adopted proper motions from Sampedro et al. (2017)

TABLE 4.2: Orbital elements for IC 166 UCAC 4. Source: Own elaboration

$\Omega_{\rm bar}$ (km s^{-1} kpc^{-1})	$\langle r_{\rm peri}\rangle$ (kpc)	$\langle r_{\rm apo}\rangle$ (kpc)	$\langle \lvert z\rvert_{\rm max}\rangle$ (kpc)	$\langle e\rangle$
		M1		
35	$10.19^{11.88}_{5.77}$	$13.39^{17.51}_{12.41}$	$0.41^{0.78}_{0.14}$	$0.20^{0.37}_{0.09}$
40	$9.40^{11.77}_{5.51}$	$13.28^{15.77}_{12.46}$	$0.44^{0.77}_{0.14}$	$0.19^{0.40}_{0.08}$
45	$9.32^{11.75}_{5.24}$	$13.29^{15.58}_{12.38}$	$0.44^{0.77}_{0.15}$	$0.18^{0.44}_{0.08}$
50	$9.21^{11.78}_{5.31}$	$13.24^{15.88}_{12.27}$	$0.45^{0.78}_{0.14}$	$0.19^{0.40}_{0.08}$
		M2		
35	$8.80^{11.67}_{3.81}$	$13.38^{17.63}_{12.35}$	$0.43^{0.78}_{0.14}$	$0.25^{0.54}_{0.10}$
40	$8.06^{11.59}_{3.71}$	$13.35^{15.73}_{12.26}$	$0.40^{0.74}_{0.13}$	$0.23^{0.57}_{0.09}$
45	$7.94^{11.53}_{3.53}$	$13.49^{15.41}_{12.34}$	$0.42^{0.74}_{0.14}$	$0.22^{0.60}_{0.09}$
50	$8.03^{11.58}_{3.67}$	$13.37^{15.37}_{12.36}$	$0.44^{0.77}_{0.14}$	$0.22^{0.58}_{0.09}$
		M3		
35	$9.99^{11.90}_{5.30}$	$13.20^{17.48}_{12.16}$	$0.39^{0.75}_{0.11}$	$0.21^{0.42}_{0.10}$
40	$9.49^{11.71}_{4.74}$	$13.22^{15.55}_{12.19}$	$0.40^{0.76}_{0.11}$	$0.19^{0.45}_{0.09}$
45	$9.48^{11.70}_{4.51}$	$13.33^{15.82}_{12.24}$	$0.41^{0.77}_{0.12}$	$0.19^{0.51}_{0.09}$
50	$9.43^{11.70}_{4.62}$	$13.29^{15.54}_{12.21}$	$0.39^{0.76}_{0.12}$	$0.20^{0.45}_{0.09}$

catalog but using the three different methods presented in their work, and both figure shows their birth positions.

The median value of the orbital parameters were found for the 10^3 realizations, as listed in Table 4.2. Uncertainties in the orbital integrations were estimates as the 16th percentile values. We define the eccentricity as:

$$e = \frac{(r_{apo} - r_{peri})}{(r_{apo} + r_{peri})},$$

where, r_{apo} is the apogalactic distance and r_{peri} the perigalactic distance. We note that uncertainties in the orbital parameters are primarily driven by the uncertainty in the proper motions, with a much smaller contribution from the uncertainty in the distance and negligible contribution from the uncertainty in the radial velocity.

On the other hand, Vande Putte et al. (2010) have recently proposed an empirical threshold to identify open clusters with possible unusual origins which is realized through the study of the cluster orbit. They found there is a correlation between the metallicity, the maximum height reached for the cluster and the η parameter which has been quantified through the radial quantity, defined as:

$$\eta = \frac{(r_{apo} - r_{peri})}{0.5(r_{apo} + r_{peri})}.$$

They also defined a threshold values for those parameters, where clusters with [Fe/H]<-0.2 dex, $|z|_{max}$>0.9 kpc and η>0.5 could have unusual origins. For IC 166 those quantities are the following: [Fe/H]=$-$0.15 dex, $|z|_{max}$ reached for the cluster is $\sim$ 0.40 kpc for every

method, while the η-parameter in every case takes usual values ($\sim$0.2) independent of the method used. Thus, independently of the method used, those threshold values confirm the galactic origin of IC 166.

The GAIA DR2 and future releases should improve the precision to which the IC 166 orbit can be calculated by providing accurate and precise proper motions.

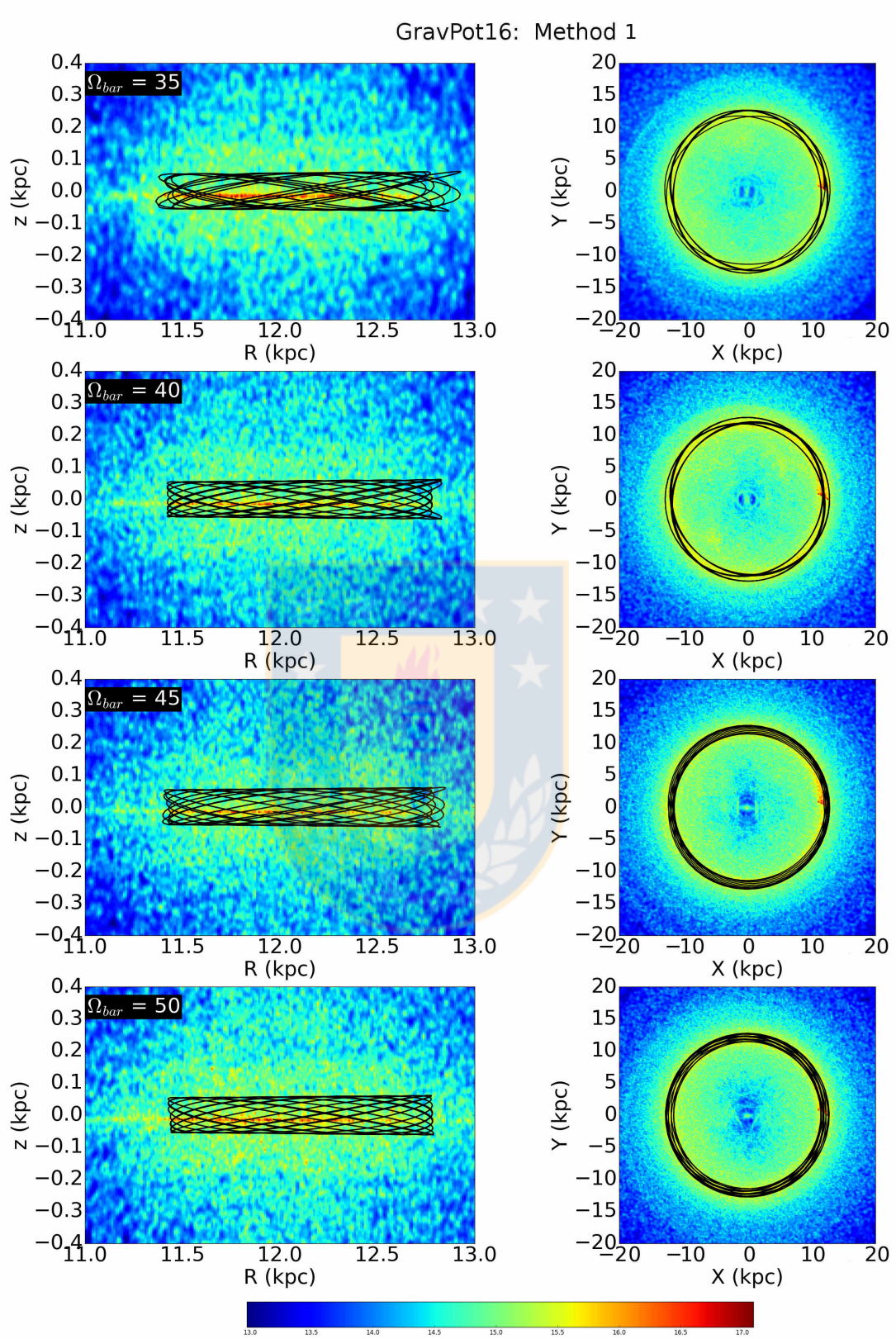

FIGURE 4.5: Probability density maps color-coded at the top for the meridional orbits in the plane R, z (column 1) and face-on (column 2) of a thousands random realizations of IC 166 time-integrated backwards for 2.5 Gyr adopting the proper motions from method 1 as described in Sampedro et al. (2017). Red and yellow colors correspond to larger probabilities. The tile size of the HealPix map is 0.10 kpc^2. The black line shows the orbit using the best values found for the cluster (see text). Source: Own elaboration

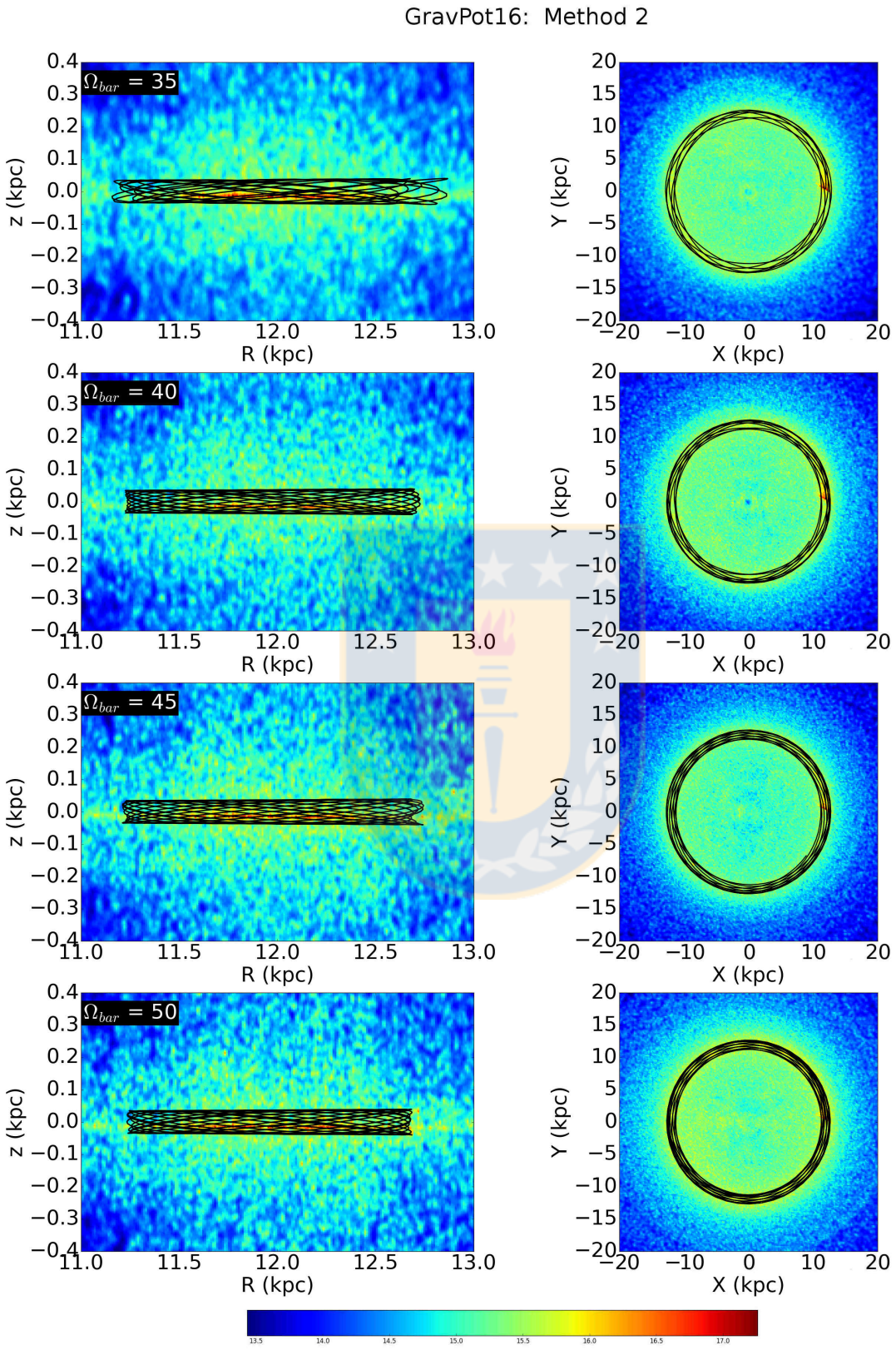

FIGURE 4.6: The same as Figure 4.5, here adopting the proper motions from method 2 as described in Sampedro et al. (2017). Source: Own elaboration

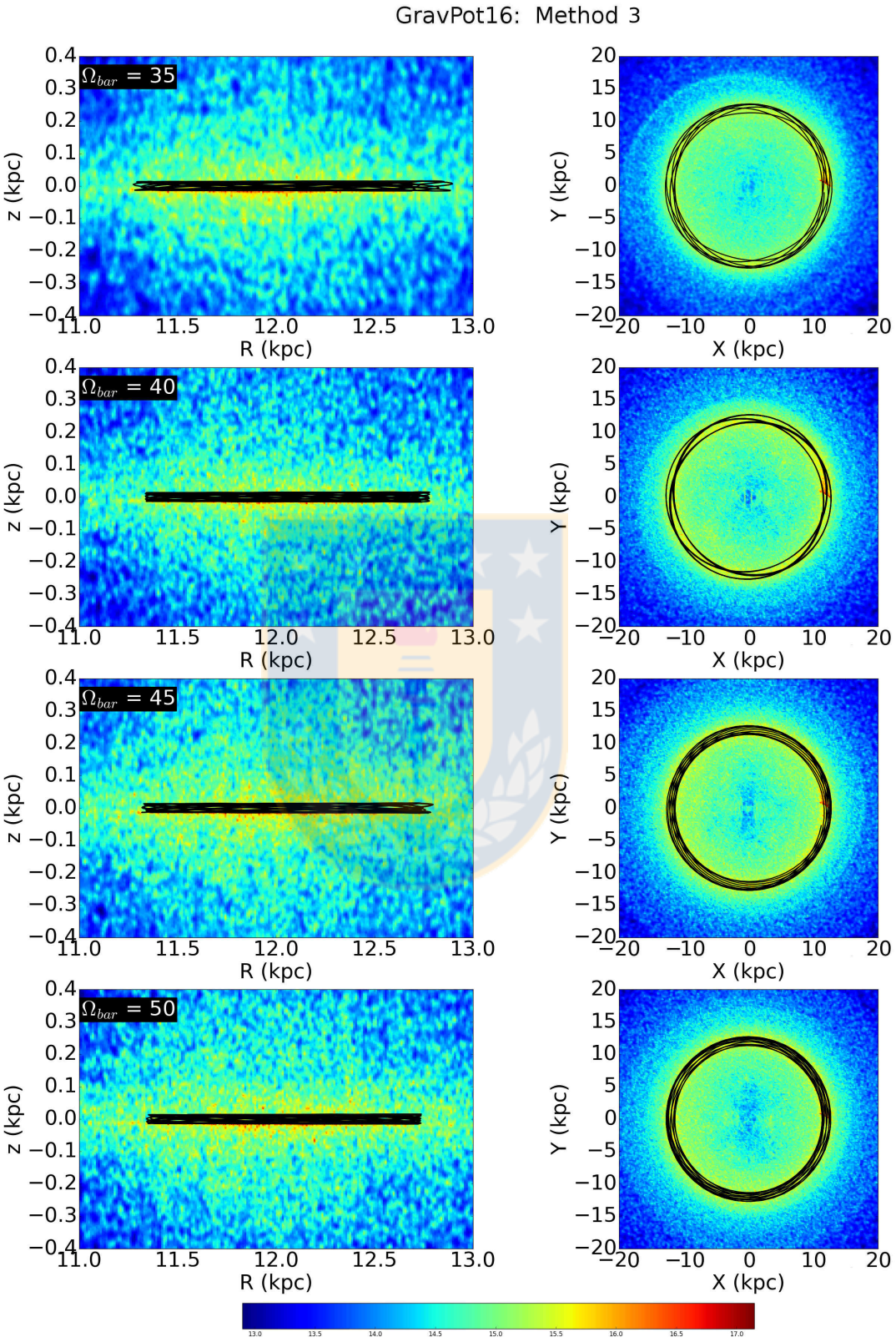

FIGURE 4.7: The same as Figure 4.5, here adopting the proper motions from method 3 as described in Sampedro et al. (2017). Source: Own elaboration

TABLE 4.3: Atomic Lines and Derived Abundances by BACCHUS using CANNON's stellar parameters. Source: Own elaboration

Element	λ_{air}	star1	star2	star3	star4	star5	star6	star7	star8	star9	star10	star11	star12	star13
Fe	15194.492	7.34	7.39	7.14	7.26	7.40	7.36	—	7.33	—	—	—	7.25	7.33
	15207.526	7.27	—	7.02	7.28	7.37	7.27	7.25	7.19	—	7.28	7.26	7.24	7.19
	15395.718	—	—	—	—	—	—	—	—	—	—	—	—	—
	15490.339	7.42	7.36	7.34	7.46	7.45	7.38	7.32	7.37	7.24	—	7.39	7.36	7.33
	15648.510	7.36	—	—	7.31	7.30	7.28	7.29	—	7.21	—	—	7.23	7.23
	15964.867	7.30	—	7.31	7.31	7.39	7.30	7.30	—	7.19	7.30	7.22	7.32	7.23
	16040.657	7.24	7.29	7.31	7.51	7.40	—	—	7.23	7.22	7.43	7.34	7.20	7.31
	16153.247	7.27	7.39	7.13	7.28	7.31	—	7.28	—	—	7.28	7.31	7.20	7.19
	16165.032	7.34	7.37	7.33	—	7.34	7.24	7.28	—	7.24	7.32	—	7.30	—
⟨A(Fe)⟩		7.32±0.06	7.36±0.04	7.23±0.13	7.34±0.10	7.37±0.05	7.30±0.05	7.29±0.02	7.28±0.08	7.22±0.02	7.32±0.06	7.30±0.07	7.26±0.06	7.26±0.06
[Fe/H]		-0.13±0.06	-0.09±0.04	-0.22±0.13	-0.11±0.10	-0.08±0.05	-0.15±0.05	-0.16±0.02	-0.17±0.08	-0.23±0.06	-0.13±0.02	-0.15±0.07	-0.19±0.06	-0.19±0.06
Mg	15740.700	7.32	7.40	7.22	7.31	7.55	7.33	7.37	—	—	7.39	7.32	7.29	—
	15748.900	7.36	7.45	7.25	7.34	7.40	7.47	7.33	7.24	7.16	7.45	—	7.27	7.35
	15765.800	7.37	7.44	7.20	7.31	7.40	7.49	7.28	7.25	7.24	7.44	7.28	—	7.30
⟨A(Mg)⟩		7.35±0.03	7.43±0.03	7.22±0.02	7.32±0.02	7.45±0.09	7.43±0.09	7.33±0.04	7.24±0.01	7.20±0.06	7.43±0.03	7.30±0.03	7.28±0.01	7.32±0.03
[Mg/Fe]		-0.05±0.03	-0.01±0.03	-0.09±0.02	-0.10±0.02	0.00±0.09	0.05±0.09	-0.04±0.04	-0.12±0.01	-0.10±0.06	0.03±0.03	-0.08±0.03	-0.06±0.01	-0.02±0.03
Ca	16136.823	—	6.06	5.96	—	—	—	—	—	—	—	—	—	—
	16150.762	—	6.30	6.21	6.16	6.26	—	—	—	6.02	6.16	—	6.10	6.14
	16155.236	—	—	—	—	—	—	—	—	—	—	—	—	—
	16157.364	6.14	—	—	6.23	6.24	—	—	—	—	6.12	—	—	—
⟨A(Ca)⟩		6.14±0.00	6.18±0.17	6.08±0.18	6.19±0.05	6.25±0.01	—	—	—	6.02±0.00	6.14±0.03	—	6.10±0.00	6.14±0.00
[Ca/Fe]		-0.04±0.00	-0.04±0.17	-0.01±0.18	-0.01±0.05	0.02±0.01	—	—	—	-0.06±0.00	-0.04±0.03	—	-0.02±0.00	0.02±0.00
K	15163.067	4.89	—	—	—	5.11	—	—	—	—	—	—	—	—
	15168.376	5.05	5.07	4.90	—	—	4.87	—	4.89	—	—	—	5.04	—
⟨A(K)⟩		4.97±0.11	5.07±0.00	4.90±0.00	—	5.11±0.00	4.87±0.00	—	4.89±0.00	—	—	—	5.03±0.00	—
[K/Fe]		0.02±0.11	0.08±0.00	0.04±0.00	—	0.11±0.00	-0.06±0.00	—	-0.02±0.00	—	—	—	0.15±0.00	—
Si	15361.100	—	—	—	—	—	—	—	—	—	—	—	—	—
	15376.800	7.31	7.46	—	—	7.43	7.42	—	7.30	—	—	7.47	7.39	—
	15557.800	7.43	7.60	7.26	7.51	7.50	7.40	7.30	—	7.23	7.29	7.28	7.32	7.30
	15884.500	—	—	—	—	—	7.19	7.24	—	—	—	—	—	—
	15960.100	7.70	—	7.50	7.58	—	7.67	7.59	—	7.51	7.60	7.52	—	7.60
	16060.000	7.66	—	—	—	—	—	—	7.38	—	—	—	7.46	—
	16094.800	7.48	7.68	7.47	—	7.56	7.40	7.44	—	7.44	7.57	—	7.59	7.47
	16129.000	—	—	—	—	—	—	—	—	—	—	—	—	—
	16163.700	—	—	—	—	—	—	—	—	—	—	—	—	—
	16170.200	—	—	—	—	—	—	—	—	—	—	—	—	—
	16215.700	7.65	7.71	—	7.47	7.61	7.55	7.50	7.37	7.29	—	7.61	—	—
	16241.800	7.60	7.71	—	7.58	7.59	—	7.46	—	7.35	7.46	—	—	7.35
	16680.800	7.44	7.43	7.31	—	7.61	7.30	7.42	—	7.21	7.50	7.49	7.37	7.40
	16828.200	—	—	—	—	7.48	—	—	7.42	7.34	7.62	—	—	—
⟨A(Si)⟩		7.53±0.14	7.60±0.12	7.38±0.12	7.53±0.05	7.54±0.07	7.42±0.16	7.42±0.12	7.37±0.05	7.34±0.11	7.51±0.12	7.47±0.12	7.43±0.10	7.42±0.12
[Si/Fe]		0.15±0.14	0.18±0.12	0.09±0.12	0.13±0.05	0.11±0.07	0.06±0.16	0.07±0.12	0.03±0.05	0.06±0.11	0.13±0.12	0.11±0.12	0.11±0.10	0.10±0.12

TABLE 4.4: Atomic Lines and Derived Abundances by BACCHUS using CANNON's stellar parameters. Second part. Source: Own elaboration

Element	λ_{air}	star1	star2	star3	star4	star5	star6	star7	star8	star9	star10	star11	star12	star13
Ti	15186.707	—	—	—	—	—	—	—	—	—	—	—	—	—
	15315.585	—	—	—	—	—	—	—	—	—	—	—	—	—
	15334.847	—	—	—	—	—	—	—	—	—	—	—	—	—
	15426.985	—	—	—	—	—	—	—	—	—	—	—	—	—
	15543.761	—	—	—	—	—	—	—	—	—	—	—	—	—
	15602.842	—	—	—	—	—	—	—	—	—	—	—	—	—
	15715.578	4.73	—	—	—	—	—	—	—	4.67	—	—	—	4.67
	16330.532	—	—	—	—	—	—	—	—	—	—	—	—	—
	16635.160	—	—	—	—	—	—	—	—	—	—	—	—	—
⟨A(Ti)⟩		4.73±0.00	—	—	—	—	—	—	—	4.67±0.00	—	—	—	4.67±0.00
[Ti/Fe]		-0.04±0.00	—	—	—	—	—	—	—	0.00±0.00	—	—	—	-0.04±0.00
Mn	15159.158	5.26	5.27	—	5.23	—	—	—	—	—	—	—	5.17	5.23
	15217.686	5.26	5.35	5.27	—	5.35	5.26	5.28	5.19	5.17	5.20	5.29	—	5.24
	15262.415	—	5.27	5.11	5.33	—	—	5.22	5.24	—	5.20	—	5.24	—
	15673.770	—	—	—	—	—	—	—	—	—	—	—	—	—
	15743.935	—	—	—	—	—	—	—	—	—	—	—	—	—
	15787.572	—	—	—	—	—	—	—	—	—	—	—	—	—
	15958.888	—	—	—	—	—	—	—	—	—	—	—	—	—
	16707.963	—	—	—	—	—	—	—	—	—	—	—	—	—
⟨A(Mn)⟩		5.26±0.00	5.30±0.05	5.19±0.11	5.28±0.07	5.35±0.00	5.26±0.00	5.25±0.04	5.21±0.03	5.17±0.00	5.20±0.00	5.29±0.00	5.20±0.05	5.23±0.01
[Mn/Fe]		0.00±0.00	0.00±0.05	0.02±0.11	0.00±0.07	0.04±0.00	0.02±0.00	0.02±0.04	-0.01±0.03	0.01±0.00	-0.06±0.00	0.05±0.00	0.00±0.05	0.03±0.01
Al	16718.957	6.55	6.48	—	—	6.50	—	6.47	6.41	6.36	6.54	—	6.35	—
	16750.564	6.38	6.49	—	6.44	6.46	6.48	6.28	6.17	6.26	6.34	6.41	6.28	6.42
	16763.359	—	—	—	—	—	—	—	—	—	—	—	—	—
⟨A(Al)⟩		6.46±0.12	6.48±0.01	—	6.44±0.00	6.48±0.03	6.48±0.00	6.37±0.13	6.29±0.17	6.31±0.07	6.44±0.14	6.41±0.00	6.31±0.05	6.42±0.00
[Al/Fe]		0.22±0.12	0.18±0.01	—	0.18±0.00	0.19±0.03	0.26±0.00	0.16±0.13	0.09±0.17	0.17±0.07	0.20±0.14	0.19±0.00	0.13±0.05	0.24±0.00

TABLE 4.5: Atomic Lines and Derived Abundances by BACCHUS using FERRE's stellar parameters. Source: Own elaboration

Element	λ_{air}	star1	star2	star3	star4	star5	star6	star7	star8	star9	star10	star11	star12	star13
Fe	15194.492	7.32	7.46	7.28	7.30	—	—	—	—	7.33	—	—	7.39	7.42
	15207.526	7.29	7.54	7.11	7.27	7.51	7.47	7.42	7.43	7.16	7.26	7.24	7.40	7.41
	15395.718	—	—	—	—	—	—	—	—	—	—	—	—	—
	15490.339	7.44	7.40	7.46	—	7.56	7.46	—	—	7.30	—	7.43	—	—
	15648.510	7.34	7.42	—	7.33	7.40	7.40	—	—	7.26	—	—	7.34	7.34
	15964.867	7.26	—	7.35	7.31	—	7.42	7.36	—	7.22	—	7.16	7.44	—
	16040.657	7.26	7.26	—	7.49	7.48	—	—	7.34	7.26	7.32	7.31	7.30	7.44
	16153.247	7.25	7.40	7.21	7.30	7.45	7.36	7.37	—	—	—	7.27	7.33	7.30
	16165.032	7.29	7.29	7.37	—	7.39	7.24	7.33	—	7.26	7.27	—	7.38	—
⟨A(Fe)⟩		7.31±0.06	7.39±0.09	7.30±0.12	7.33±0.08	7.46±0.06	7.39±0.08	7.37±0.04	7.38±0.06	7.26±0.05	7.28±0.03	7.28±0.10	7.37±0.05	7.38±0.06
[Fe/H]		-0.14±0.06	-0.06±0.09	-0.15±0.12	-0.12±0.08	0.01±0.06	-0.06±0.08	-0.08±0.04	-0.07±0.06	-0.19±0.05	-0.17±0.00	-0.17±0.10	-0.08±0.05	-0.07±0.06
Mg	15740.700	7.26	7.26	7.26	7.27	7.37	7.25	7.38	—	7.17	—	7.21	7.38	7.24
	15748.900	7.26	7.29	7.25	7.23	7.32	7.28	7.30	—	7.10	—	7.35	7.29	7.31
	15765.800	7.27	7.23	7.22	7.21	7.31	7.33	7.22	—	7.13	—	—	—	—
⟨A(Mg)⟩		7.26±0.01	7.26±0.03	7.24±0.02	7.24±0.03	7.33±0.03	7.29±0.04	7.30±0.08	—	7.13±0.03	—	7.28±0.10	7.33±0.06	7.27±0.05
[Mg/Fe]		-0.13±0.01	-0.21±0.03	-0.14±0.02	-0.17±0.03	-0.21±0.03	-0.18±0.04	-0.15±0.08	—	-0.21±0.03	—	-0.08±0.10	-0.12±0.06	-0.19±0.05
Ca	16136.823	—	6.07	6.01	—	—	—	—	—	—	—	—	—	—
	16150.762	6.05	6.28	6.27	6.15	6.28	—	—	—	6.02	6.04	—	6.18	6.14
	16155.236	—	—	—	—	—	—	—	—	—	—	—	—	—
	16157.364	6.11	—	—	—	6.32	—	—	—	—	—	—	—	—
⟨A(Ca)⟩		6.08±0.04	6.17±0.15	6.14±0.18	6.15±0.00	6.30±0.03	—	—	—	6.02±0.00	6.04±0.00	—	6.18±0.00	6.14±0.00
[Ca/Fe]		-0.09±0.04	-0.08±0.15	-0.02±0.18	-0.04±0.00	-0.02±0.03	—	—	—	-0.10±0.00	-0.10±0.00	—	-0.05±0.00	-0.10±0.00
K	15163.067	4.82	—	—	—	5.15	—	5.03	—	—	—	—	—	—
	15168.376	4.95	5.08	4.95	—	5.17	4.92	—	—	—	—	—	5.15	—
⟨A(K)⟩		4.88±0.09	5.08±0.00	4.95±0.00	—	5.16±0.01	4.92±0.00	5.03±0.00	—	—	—	—	5.15±0.00	—
[K/Fe]		-0.06±0.09	0.06±0.00	0.02±0.00	—	0.07±0.01	-0.10±0.00	0.03±0.00	—	—	—	—	0.15±0.00	—
Si	15361.100	—	—	—	—	—	—	—	—	—	—	—	—	—
	15376.800	7.31	7.46	—	—	7.50	7.56	—	7.37	—	—	7.40	7.47	—
	15557.800	7.40	—	—	7.53	7.60	7.56	7.40	—	7.32	—	7.34	—	7.42
	15884.500	—	—	—	—	—	—	—	—	—	—	—	—	—
	15960.100	7.63	—	7.52	7.51	7.76	7.57	7.59	—	7.48	7.53	7.40	7.88	7.60
	16060.000	—	—	—	7.74	—	—	—	7.46	—	—	—	7.55	—
	16094.800	—	7.56	7.49	—	7.56	7.40	7.43	—	7.43	7.50	7.30	7.60	7.51
	16129.000	—	—	—	—	—	—	—	—	—	—	—	—	—
	16163.700	—	—	—	—	—	—	—	—	—	—	—	—	—
	16170.200	—	—	—	—	—	—	—	—	—	—	—	—	—
	16215.700	—	7.70	—	7.48	7.71	7.69	7.60	—	7.37	—	—	—	—
	16241.800	—	7.70	—	7.59	7.61	—	7.58	7.47	—	—	7.53	7.38	—
	16680.800	7.46	7.37	7.36	—	7.69	7.41	7.52	7.44	7.27	7.49	7.43	7.44	7.58
	16828.200	—	—	—	—	—	—	—	—	7.32	—	—	—	—
⟨A(Si)⟩		7.45±0.13	7.56±0.15	7.46±0.08	7.53±0.05	7.63±0.09	7.53±0.11	7.52±0.09	7.43±0.04	7.36±0.08	7.51±0.02	7.40±0.08	7.55±0.18	7.53±0.08
[Si/Fe]		0.08±0.13	0.11±0.15	0.10±0.08	0.14±0.05	0.11±0.09	0.08±0.11	0.09±0.09	-0.01±0.04	0.04±0.08	0.17±0.02	0.06±0.08	0.12±0.18	0.09±0.08

TABLE 4.6: Atomic Lines and Derived Abundances by BACCHUS using FERRE's stellar parameters. Second part. Source: Own elaboration

Element	λ_{air}	star1	star2	star3	star4	star5	star6	star7	star8	star9	star10	star11	star12	star13
Ti	15186.707	—	—	—	—	—	—	—	—	—	—	—	—	—
	15315.585	—	—	—	—	—	—	—	—	—	—	—	—	—
	15334.847	—	—	—	—	—	—	—	—	—	—	—	—	—
	15426.985	—	—	—	—	—	—	—	—	—	—	—	—	—
	15543.761	—	—	—	—	—	—	—	—	—	—	—	—	—
	15602.842	—	—	—	—	—	—	—	—	—	—	—	—	—
	15715.578	4.69	—	—	—	—	—	—	—	—	—	—	—	4.81
	16330.532	—	—	—	—	—	—	—	—	—	—	—	—	—
	16635.160	—	—	—	—	—	—	—	—	—	—	—	—	—
⟨A(Ti)⟩		4.69±0.00	—	—	—-	—	—	—	—	—	—	—	—	4.81±0.00
[Ti/Fe]		-0.07±0.00	—	—	—	—	—	—	—	—	—	—	—	-0.02±0.00
Mn	15159.158	5.21	5.29	—	5.25	—	5.33	—	—	—	—	—	—	—
	15217.686	—	5.38	5.35	5.24	5.38	5.32	5.32	—	5.18	—	5.27	—	5.27
	15262.415	—	5.29	5.18	5.35	—	5.31	5.25	—	5.30	—	—	5.34	—
	15673.770	—	—	—	—	—	—	—	—	—	—	—	—	5.37
	15743.935	—	—	—	—	—	—	—	—	—	—	—	—	—
	15787.572	—	—	—	—	—	—	—	—	—	—	—	—	—
	15958.888	—	—	—	—	—	—	—	—	—	—	—	—	—
	16707.963	—	—	—	—	—	—	—	—	—	—	—	—	—
⟨A(Mn)⟩		5.21±0.00	5.32±0.05	5.26±0.12	5.28±0.06	5.38±0.00	5.32±0.01	5.28±0.05	—	5.24±0.08	—	5.27±0.00	5.34±0.00	5.32±0.07
[Mn/Fe]		-0.04±0.00	-0.01±0.05	0.02±0.12	0.01±0.06	-0.02±0.00	-0.01±0.01	-0.03±0.05	—	0.04±0.08	—	0.05±0.00	0.03±0.00	0.00±0.07
Al	16718.957	6.51	6.40	—	—	6.52	—	6.50	6.50	6.36	—	—	6.46	—
	16750.564	6.39	6.43	—	6.38	6.49	6.44	6.34	6.27	6.24	6.38	6.37	6.39	6.51
	16763.359	—	—	—	—	—	—	—	—	—	—	—	—	—
⟨A(Al)⟩		6.45±0.08	6.41±0.02	—	6.38±0.00	6.50±0.02	6.44±0.00	6.42±0.11	6.38±0.16	6.30±0.08	6.38±0.00	6.37±0.00	6.42±0.05	6.51±0.00
[Al/Fe]		0.22±0.08	0.10±0.02	—	0.13±0.00	0.12±0.02	0.13±0.00	0.13±0.11	0.08±0.16	0.12±0.08	0.18±0.00	0.17±0.00	0.13±0.05	0.21±0.00

Chapter 5

Discusion and Conclusions

We have analyzed 13 APOGEE spectra manually through the BACCHUS code using two different sets of stellar parameters provided from *The CANNON* and FEREE codes. Additionally, we also explore the kinematics of the cluster using the galactic dynamic software GravPot16, in order to constrain the possible origin of the cluster from the dynamical point of view. In this way the first chemical and dynamic study of IC 166 was performed. The salient results are:

- Based on their spatial location, RV, metallicity, CMD position and proper motions, we have selected 13 likely members of IC 166.
- A manual chemical analysis was done using BACCHUS with two different sets of stellar parameters. We are able to reduce the dispersion found by ASPCAP in some species (Si, Ca, Ti, Al), but increase it in the case of Fe and Mg. The most notable improvement is for Al.
- We find good agreement between our abundances and general galactic trends from large scale studies, as well as the metallicity gradient.
- According to our results, the cluster follows the low-sequence in the [α/Fe] vs [Fe/H] plane which is a chemical signature of its belonging to the thin disk of the MW.
- We used the galactic dynamic software GravPot16 (Férnandez-Trincado et al., in prep.) to study the kinematics of IC 166. We found that the cluster has always been confined to the thin disk along its orbit.
- Additionally, using the empirical relation found by Vande Putte et al. (2010) between [Fe/H], η parameter and $|z|_{max}$, we confirm the galactic origin of IC 166.

Bibliography

Allende Prieto C., Beers T. C., Wilhelm R., Newberg H. J., Rockosi C. M., Yanny B., Lee Y. S., 2006, ApJ, 636, 804

Alvarez R., Plez B., 1998, A&A, 330, 1109

Arnould M., Goriely S., Jorissen A., 1999, A&A, 347, 572

Asplund M., Grevesse N., Sauval A. J., 2005, in Barnes III T. G., Bash F. N., eds, Cosmic Abundances as Records of Stellar Evolution and Nucleosynthesis Vol. 336 of Astronomical Society of the Pacific Conference Series, The Solar Chemical Composition. p. 25

Battistini C., Bensby T., 2015, A&A, 577, A9

Bensby T., Feltzing S., Lundström I., Ilyin I., 2005, A&A, 433, 185

Bensby T., Feltzing S., Oey M. S., 2014, A&A, 562, A71

Bonatto C., Kerber L. O., Bica E., Santiago B. X., 2006, A&A, 446, 121

Bowen I. S., Vaughan Jr. A. H., 1973, ao, 12, 1430

Bressan A., Marigo P., Girardi L., Salasnich B., Dal Cero C., Rubele S., Nanni A., 2012, MNRAS, 427, 127

Brunthaler A., Reid M. J., Menten K. M., Zheng X.-W., Bartkiewicz A., Choi Y. K., Dame T., Hachisuka K., Immer K., Moellenbrock G., Moscadelli L., Rygl K. L. J., Sanna A., Sato M., Wu Y., Xu Y., Zhang B., 2011, Astronomische Nachrichten, 332, 461

Burkhead M. S., 1969, AJ, 74, 1171

Carretta E., Bragaglia A., Gratton R. G., Lucatello S., Catanzaro G., Leone F., Bellazzini M., Claudi R., D'Orazi V., Momany Y., Ortolani S., Pancino E., Piotto G., Recio-Blanco A., Sabbi E., 2009, A&A, 505, 117

Carretta E., Bragaglia A., Gratton R. G., Recio-Blanco A., Lucatello S., D'Orazi V., Cassisi S., 2010, A&A, 516, A55

Chen Y. Q., Nissen P. E., Zhao G., Zhang H. W., Benoni T., 2000, A&AS, 141, 491

Clayton D., 2007, Handbook of Isotopes in the Cosmos

Cunha K., Frinchaboy P. M., Souto D., Thompson B., Zasowski G., Allende Prieto C., Carrera R., Chiappini C., Donor J., García-Hernández D. A., García Pérez A. E., Hayden M. R., Holtzman J., et al. 2016, Astronomische Nachrichten, 337, 922

De Silva G. M., Freeman K. C., Bland-Hawthorn J., Martell S., de Boer E. W., Asplund M., Keller S., Sharma S., Zucker D. B., Zwitter T., Anguiano B., Bacigalupo C., Bayliss D., Beavis M. A., Bergemann M., 2015, MNRAS, 449, 2604

Dias W. S., Alessi B. S., Moitinho A., Lépine J. R. D., 2002, A&A, 389, 871

Dias W. S., Monteiro H., Caetano T. C., Lépine J. R. D., Assafin M., Oliveira A. F., 2014, A&A, 564, A79

Donati P., Cantat Gaudin T., Bragaglia A., Friel E., Magrini L., Smiljanic R., Vallenari A., Tosi M., Sordo R., Tautvaišienė G., Blanco-Cuaresma S., Costado M. T., 2014, A&A, 561, A94

Fernández-Trincado J. G., Geisler D., Moreno E., Zamora O., Robin A. C., Villanova S., 2017, ArXiv e-prints

Fernández-Trincado J. G., Robin A. C., Moreno E., Pérez-Villegas A., Pichardo B., 2017, ArXiv e-prints

Fernández-Trincado J. G., Robin A. C., Moreno E., Schiavon R. P., García Pérez A. E., Vieira K., Cunha K., Zamora O., Sneden C., Souto D., 2016, ApJ, 833, 132

Fleming S. W., Mahadevan S., Deshpande R., Bender C. F., Terrien R. C., Marchwinski R. C., Wang J., Roy A., 2015, AJ, 149, 143

Friel E. D., 1995, ARA&A, 33, 381

Friel E. D., 2013, Open Clusters and Their Role in the Galaxy. p. 347

Friel E. D., Donati P., Bragaglia A., Jacobson H. R., Magrini L., Prisinzano L., Randich S., Tosi M., Cantat-Gaudin T., Vallenari A., Smiljanic R., Carraro G., Sordo R., 2014, A&A, 563, A117

Friel E. D., Janes K. A., 1993, A&A, 267, 75

Friel E. D., Liu T., Janes K. A., 1989, PASP, 101, 1105

Frinchaboy P. M., Thompson B., Jackson K. M., O'Connell J., Meyer B., Zasowski G., Majewski S. R., Chojnowksi S. D., Johnson J. A., Allende Prieto C., 2013, ApJL, 777, L1

García Pérez A. E., Allende Prieto C., Holtzman J. A., Shetrone M., Mészáros S., Bizyaev D., Carrera R., 2016, AJ, 151, 144

García Pérez A. E., Allende Prieto C., Holtzman J. A., Shetrone M., Mészáros S., Bizyaev D., Carrera R., Cunha K., García-Hernández D. A., 2016, AJ, 151, 144

Gieles M., Portegies Zwart S. F., Baumgardt H., Athanassoula E., Lamers H. J. G. L. M., Sipior M., Leenaarts J., 2006, MNRAS, 371, 793

Gilmore G., Randich S., Asplund M., Binney J., Bonifacio P., Drew J., Feltzing S., Ferguson A., Jeffries R., Micela G., et al. 2012, The Messenger, 147, 25

Gunn J. E., Siegmund W. A., Mannery E. J., Owen R. E., Hull C. L., 2006, AJ, 131, 2332

Gustafsson B., Edvardsson B., Eriksson K., Jørgensen U. G., Nordlund Å., Plez B., 2008, A&A, 486, 951

Hawkins K., Masseron T., Jofré P., Gilmore G., Elsworth Y., Hekker S., 2016, A&A, 594, A43

Hayden M. R., Bovy J., Holtzman J. A., Nidever D. L., Bird J. C., Weinberg D. H., Andrews B. H., Majewski S. R., Allende Prieto C., Anders F., 2015, ApJ, 808, 132

Holtzman J. A., Shetrone M., Johnson J. A., Allende Prieto C., Anders F., Andrews B., Beers T. C., Bizyaev D., Blanton M. R., Bovy J., Carrera R., Chojnowski S. D., Cunha K., 2015, AJ, 150, 148

Hurley J. R., Pols O. R., Aarseth S. J., Tout C. A., 2005, MNRAS, 363, 293

Jacobson H. R., Friel E. D., Jílková L., Magrini L., Bragaglia A., Vallenari A., Tosi M., Randich S., Donati P., Cantat-Gaudin T., 2016, A&A, 591, A37

Janes K. A., Tilley C., Lynga G., 1988, AJ, 95, 771

Kharchenko N. V., Piskunov A. E., Schilbach E., Röser S., Scholz R.-D., 2012, A&A, 543, A156

Kordopatis G., Wyse R. F. G., Gilmore G., Recio-Blanco A., de Laverny P., Hill V., Adibekyan V., Heiter U., Minchev I., Famaey B., 2015, A&A, 582, A122

Kurucz R. L., 1970, SAO Special Report, 309

Lada C. J., Lada E. A., 2003, ARA&A, 41, 57

Lamers H. J. G. L. M., Gieles M., 2006, A&A, 455, L17

Lamers H. J. G. L. M., Gieles M., Bastian N., Baumgardt H., Kharchenko N. V., Portegies Zwart S., 2005, A&A, 441, 117

Linden S. T., Pryal M., Hayes C. R., Troup N. W., Majewski S. R., Andrews B. H., Beers T. C., Carrera R., Cunha K., 2017, ApJ, 842, 49

Loktin A. V., Beshenov G. V., 2003, Astronomy Reports, 47, 6

Magrini L., Randich S., Donati P., Bragaglia A., Adibekyan V., Romano D., Smiljanic R., Blanco-Cuaresma S., Tautvaišienė G., Friel E., Overbeek J., Jacobson H., Cantat-Gaudin T., 2015, A&A, 580, A85

Magrini L., Sestito P., Randich S., Galli D., 2009, A&A, 494, 95

Majewski S. R., Schiavon R. P., Frinchaboy P. M., Allende Prieto C., Barkhouser R., Bizyaev D., Blank B., Brunner S., Burton A., Carrera R., Chojnowski S. D., Cunha K., Epstein C., 2017, AJ, 154, 94

Masseron T., Gilmore G., 2015, MNRAS, 453, 1855

Masseron T., Merle T., Hawkins K., , 2016, BACCHUS: Brussels Automatic Code for Characterizing High accUracy Spectra, Astrophysics Source Code Library

Mathieu R. D., 1984, ApJ, 284, 643

Monari G., Famaey B., Siebert A., Duchateau A., Lorscheider T., Bienaymé O., 2017, MNRAS, 465, 1443

Monari G., Kawata D., Hunt J. A. S., Famaey B., 2017, MNRAS, 466, L113

Moraux E., Kroupa P., Bouvier J., 2004, A&A, 426, 75

Ness M., Hogg D. W., Rix H.-W., Ho A. Y. Q., Zasowski G., 2015, ApJ, 808, 16

Plez B., , 2012, Turbospectrum: Code for spectral synthesis, Astrophysics Source Code Library

Portail M., Gerhard O., Wegg C., Ness M., 2017, MNRAS, 465, 1621

Randich S., Gilmore G., Gaia-ESO Consortium 2013, The Messenger, 154, 47

Robin A. C., Marshall D. J., Schultheis M., Reylé C., 2012, A&A, 538, A106

Robin A. C., Reylé C., Derrière S., Picaud S., 2003, A&A, 409, 523

Robin A. C., Reylé C., Fliri J., Czekaj M., Robert C. P., Martins A. M. M., 2014, A&A, 569, A13

Samland M., 1998, ApJ, 496, 155

Sampedro L., Dias W. S., Alfaro E. J., Monteiro H., Molino A., 2017, MNRAS, 470, 3937

Sandage A., 1957, ApJ, 125, 435

Schönrich R., Binney J., Dehnen W., 2010, MNRAS, 403, 1829

Souto D., Cunha K., Smith V., Allende Prieto C., Pinsonneault M., Zamora O., García-Hernández D. A., Mészáros S., Bovy J., 2016, ApJ, 830, 35

Spitzer Jr. L., 1958, ApJ, 127, 17

Subramaniam A., Bhatt B. C., 2007, MNRAS, 377, 829

Tang B., Cohen R. E., Geisler D., Schiavon R. P., 2017, MNRAS, 465, 19

Trumpler R. J., 1930, Lick Observatory Bulletin, 14, 154

Twarog B. A., Ashman K. M., Anthony-Twarog B. J., 1997, AJ, 114, 2556

Vallenari A., Carraro G., Richichi A., 2000, A&A, 353, 147

van den Bergh S., 2006, AJ, 131, 1559

Vande Putte D., Garnier T. P., Ferreras I., Mignani R. P., Cropper M., 2010, MNRAS, 407, 2109

Woosley S. E., Weaver T. A., 1995, ApJS, 101, 181

Zacharias N., Finch C. T., Girard T. M., Henden A., Bartlett J. L., Monet D. G., Zacharias M. I., 2013, AJ, 145, 44

Zhang H. W., Gehren T., Butler K., Shi J. R., Zhao G., 2006, A&A, 457, 645